Astronomy & Astrophysics manuscript no. DL07˙Planck˙final˙arxiv
February 17, 2016

Planck intermediate results. XXIX. All-sky dust modelling with *Planck*, *IRAS*, and *WISE* observations

Planck Collaboration: P. A. R. Ade[78], N. Aghanim[54], M. I. R. Alves[54], G. Aniano[54] *, M. Arnaud[66], M. Ashdown[63,5], J. Aumont[54], C. Baccigalupi[77], A. J. Banday[84,9], R. B. Barreiro[60], N. Bartolo[27], E. Battaner[86,87], K. Benabed[55,83], A. Benoit-Lévy[21,55,83], J.-P. Bernard[84,9], M. Bersanelli[30,46], P. Bielewicz[84,9,77], A. Bonaldi[62], L. Bonavera[60], J. R. Bond[8], J. Borrill[12,80], F. R. Bouchet[55,83], F. Boulanger[54], C. Burigana[45,28,47], R. C. Butler[45], E. Calabrese[82], J.-F. Cardoso[67,1,55], A. Catalano[68,65], A. Chamballu[66,14,54], H. C. Chiang[24,6], P. R. Christensen[74,33], D. L. Clements[51], S. Colombi[55,83], L. P. L. Colombo[20,61], F. Couchot[64], B. P. Crill[61,75], A. Curto[5,60], F. Cuttaia[45], L. Danese[77], R. D. Davies[62], R. J. Davis[62], P. de Bernardis[29], A. de Rosa[45], G. de Zotti[42,77], J. Delabrouille[1], C. Dickinson[62], J. M. Diego[60], H. Dole[54,53], S. Donzelli[46], O. Doré[61,10], M. Douspis[54], B. T. Draine[76], A. Ducout[55,51], X. Dupac[36], G. Efstathiou[57], F. Elsner[55,83], T. A. Enßlin[71], H. K. Eriksen[58], E. Falgarone[65], F. Finelli[45,47], O. Forni[84,9], M. Frailis[44], A. A. Fraisse[24], E. Franceschi[45], A. Frejsel[74], S. Galeotta[44], S. Galli[55], K. Ganga[1], T. Ghosh[54], M. Giard[84,9], E. Gjerløw[58], J. González-Nuevo[60,77], K. M. Górski[61,88], A. Gregorio[31,44,49], A. Gruppuso[45], V. Guillet[54], F. K. Hansen[58], D. Hanson[72,61,8], D. L. Harrison[57,63], S. Henrot-Versillé[64], C. Hernández-Monteagudo[11,71], D. Herranz[60], S. R. Hildebrandt[10], E. Hivon[55,83], W. A. Holmes[61], W. Hovest[71], K. M. Huffenberger[22], G. Hurier[54], A. H. Jaffe[51], T. R. Jaffe[84,9], W. C. Jones[24], E. Keihänen[23], R. Keskitalo[12], T. S. Kisner[70], R. Kneissl[35,7], J. Knoche[71], M. Kunz[16,54,2], H. Kurki-Suonio[23,40], G. Lagache[54], J.-M. Lamarre[65], A. Lasenby[5,63], M. Lattanzi[28], C. R. Lawrence[61], R. Leonardi[36], F. Levrier[65], M. Liguori[27], P. B. Lilje[58], M. Linden-Vørnle[15], M. López-Caniego[60], P. M. Lubin[25], J. F. Macías-Pérez[68], B. Maffei[62], D. Maino[30,46], N. Mandolesi[45,4,28], M. Maris[44], D. J. Marshall[66], P. G. Martin[8], E. Martínez-González[60], S. Masi[29], S. Matarrese[27], P. Mazzotta[32], A. Melchiorri[29,48], L. Mendes[36], A. Mennella[30,46], M. Migliaccio[57,63], M.-A. Miville-Deschênes[54,8], A. Moneti[55], L. Montier[84,9], G. Morgante[45], D. Mortlock[51], D. Munshi[78], J. A. Murphy[73], P. Naselsky[74,33], P. Natoli[28,3,45], H. U. Nørgaard-Nielsen[15], D. Novikov[51], I. Novikov[74], C. A. Oxborrow[15], L. Pagano[29,48], F. Pajot[54], R. Paladini[52], D. Paoletti[45,47], F. Pasian[44], O. Perdereau[64], L. Perotto[68], F. Perrotta[77], V. Pettorino[39], F. Piacentini[29], M. Piat[1], S. Plaszczynski[64], E. Pointecouteau[84,9], G. Polenta[3,43], N. Ponthieu[54,50], L. Popa[56], G. W. Pratt[66], S. Prunet[55,83], J.-L. Puget[54], J. P. Rachen[18,71], W. T. Reach[85], R. Rebolo[59,13,34], M. Reinecke[71], M. Remazeilles[62,54,1], C. Renault[68], I. Ristorcelli[84,9], G. Rocha[61,10], G. Roudier[1,65,61], J. A. Rubiño-Martín[59,34], B. Rusholme[52], M. Sandri[45], D. Santos[68], D. Scott[19], L. D. Spencer[78], V. Stolyarov[5,63,81], R. Sudiwala[78], R. Sunyaev[71,79], D. Sutton[57,63], A.-S. Suur-Uski[23,40], J.-F. Sygnet[55], J. A. Tauber[37], L. Terenzi[38,45], L. Toffolatti[17,60,45], M. Tomasi[30,46], M. Tristram[64], M. Tucci[16,64], G. Umana[41], L. Valenziano[45], J. Valiviita[23,40], B. Van Tent[69], P. Vielva[60], F. Villa[45], L. A. Wade[61], B. D. Wandelt[55,83,26], I. K. Wehus[61], N. Ysard[23], D. Yvon[14], A. Zacchei[44], and A. Zonca[25]

(Affiliations can be found after the references)

Preprint online version: February 17, 2016

ABSTRACT

We present all-sky modelling of the high resolution *Planck*, *IRAS*, and *WISE* infrared (IR) observations using the physical dust model presented by Draine & Li in 2007 (DL). We study the performance and results of this model, and discuss implications for future dust modelling. The present work extends the DL dust modelling carried out on nearby galaxies using *Herschel* and *Spitzer* data to Galactic dust emission. We employ the DL dust model to generate maps of the dust mass surface density Σ_{M_d}, the dust optical extinction A_V, and the starlight intensity heating the bulk of the dust, parametrized by $U_{\rm min}$. The DL model reproduces the observed spectral energy distribution (SED) satisfactorily over most of the sky, with small deviations in the inner Galactic disk and in low ecliptic latitude areas, presumably due to zodiacal light contamination. In the Andromeda galaxy (M31), the present dust mass estimates agree remarkably well (within 10 %) with DL estimates based on independent *Spitzer* and *Herschel* data. We compare the DL optical extinction A_V for the diffuse interstellar medium (ISM) with optical estimates for approximately 2×10^5 quasi-stellar objects (QSOs) observed in the Sloan digital sky survey (SDSS). The DL A_V estimates are larger than those determined towards QSOs by a factor of about 2, which depends on $U_{\rm min}$. The DL fitting parameter $U_{\rm min}$, effectively determined by the wavelength where the SED peaks, appears to trace variations in the far-IR opacity of the dust grains per unit A_V, and not only in the starlight intensity. These results show that some of the physical assumptions of the DL model will need to be revised. To circumvent the model deficiency, we propose an empirical renormalization of the DL A_V estimate, dependent of $U_{\rm min}$, which compensates for the systematic differences found with QSO observations. This renormalization, made to match the A_V estimates towards QSOs, also brings into agreement the DL A_V estimates with those derived for molecular clouds from the near-IR colours of stars in the 2 micron all sky survey (2MASS). The DL model and the QSOs data are also used to compress the spectral information in the *Planck* and *IRAS* observations for the diffuse ISM to a family of 20 SEDs normalized per A_V, parameterized by $U_{\rm min}$, which may be used to test and empirically calibrate dust models. The family of SEDs and the maps generated with the DL model are made public in the *Planck* Legacy Archive.

Key words. ISM: general – Galaxy: general – submillimeter: ISM

1. Introduction

Studying the interstellar medium (ISM) is important in a wide range of astronomical disciplines, from star and planet formation to galaxy evolution. Dust changes the appearance of galaxies by

* Corresponding authors: gonzalo.aniano@ias.u-psud.fr and francois.boulanger@ias.u-psud.fr

absorbing ultraviolet (UV), optical, and infrared (IR) starlight, and emitting mid-IR and far-IR (FIR) radiation. Dust is an important agent in the chemical and thermodynamical evolution of the ISM. Physical models of interstellar dust that have been developed are constrained by such observations. In the present work, we study the ability of a physical dust model to reproduce IR emission and optical extinction observations, using the newly available *Planck*[1] data.

The *Planck* data provide a full-sky view of the Milky Way (MW) at submillimetre (submm) wavelengths, with much higher angular resolution than earlier maps made by the Diffuse Infrared Background Experiment (DIRBE) (Silverberg et al. 1993) on the *Cosmic background explorer* (*COBE*) spacecraft (Boggess et al. 1992). These new constraints on the spectral energy distribution (SED) emission of large dust grains were modelled by Planck Collaboration XI (2014, hereafter *Pl*-MBB) using a modified blackbody (MBB) spectral model, parameterized by optical depth and dust temperature. That study, along with previous *Planck* results, confirmed spatial changes in the dust submm opacity even in the high latitude sky (Planck Collaboration XXIV 2011; Planck Collaboration Int. XVII 2014). The dust temperature, which reflects the thermal equilibrium, is anti-correlated with the FIR opacity. The dust temperature is also affected by the strength of the interstellar radiation field (ISRF) heating the dust. The bolometric emission per H atom is almost constant at high latitude, consistent with a uniform ISRF, but over the full sky, covering lines of sight through the Galaxy, the ISRF certainly changes. The all-sky submm dust optical depth was also calibrated in terms of optical extinction. However, no attempt was made to connect these data with a self-consistent dust model, which is the goal of this complementary paper.

Several authors have modelled the dust absorption and emission in the diffuse ISM, e.g. Draine & Lee (1984); Desert et al. (1990); Dwek (1998); Zubko et al. (2004); Compiègne et al. (2011); Jones et al. (2013); Siebenmorgen et al. (2014). We focus on one of the most widely used dust models presented by Draine & Li (2007, hereafter DL). Earlier, Draine & Lee (1984) studied the optical properties of graphite and silicate dust grains, while Weingartner & Draine (2001) and Li & Draine (2001) developed a carbonaceous-silicate grain model that has been quite successful in reproducing observed interstellar extinction, scattering, and IR emission. DL presented an updated physical dust model, extensively used to model starlight absorption and IR emission. The DL dust model employs a mixture of amorphous silicate grains and carbonaceous grains. The grains are assumed to be heated by a distribution of starlight intensities. The model assumes optical properties of the dust grains and the model SEDs are computed from first principles.

The DL model has been successfully employed to study the ISM in a variety of galaxies. Draine et al. (2007) employed DL to estimate the dust masses, abundances of polycyclic aromatic hydrocarbon (PAH) molecules, and starlight intensities in the *Spitzer* Infrared Nearby Galaxies Survey – Physics of the Star-Forming ISM and Galaxy Evolution (SINGS, Kennicutt et al. 2003) galaxy sample. This survey observed a sample of 75 nearby (within 30 Mpc of the Galaxy) galaxies, covering the full range in a three-dimensional parameter space of physical properties, with the *Spitzer Space Telescope* (Werner et al. 2004). The Key Insights on Nearby Galaxies: a FIR Survey with *Herschel* (KINGFISH, Kennicutt et al. 2011) project, additionally observed a subsample of 61 of the SINGS galaxies with the *Herschel Space Observatory* (Pilbratt et al. 2010). Aniano et al. (2012) presented a detailed resolved study of two KINGFISH galaxies, NGC 628 and NGC 6946, using the DL model constrained by *Spitzer* and *Herschel* photometry. Aniano et al. (2015) extended the preceding study to the full KINGFISH sample of galaxies. Draine et al. (2014, hereafter DA14), presented a resolved study of the nearby Andromeda galaxy (M31), where high spatial resolution can be achieved. The DL model proved able to reproduce the observed emission from dust in the KINGFISH galaxies and M31. Ciesla et al. (2014) used the DL model to fit the volume limited, K-band selected sample of galaxies of the *Herschel* Reference Survey (Boselli et al. 2010), finding it systematically underestimated the 500 μm photometry.

The new *Planck* all-sky maps, combined with ancillary *Infrared Astronomical Satellite* (*IRAS*, Neugebauer et al. 1984) and *Wide-field Infrared Survey Explorer* (*WISE*, Wright et al. 2010) maps allow us to explore the dust thermal emission from the MW ISM with greater spatial resolution and frequency coverage than ever before. Here we test the compatibility of the DL dust model with these new observations.

We employ *WISE* 12[2] (12 μm), *IRAS* 60 (60 μm), *IRAS* 100 (100 μm), *Planck* 857 (350 μm), *Planck* 545 (550 μm), and *Planck* 353 (850 μm) maps to constrain the dust emission SED in the range 10 μm $< \lambda <$ 970 μm. These data allow us to generate reliable maps of the dust emission using a Gaussian point spread function (PSF) with 5′ full width at half maximum (FWHM). Working at lower resolution (1° FWHM), we can add the DIRBE 140 and DIRBE 240 photometric constraints.

We employ the DL dust model to characterize:

- the dust mass surface density Σ_{M_d};
- the dust optical extinction A_V;
- the dust mass fraction in small PAH grains q_PAH;
- the fraction of the total luminosity radiated by dust that arises from dust heated by intense radiation fields, f_PDR;
- the starlight intensity U_min heating the bulk of the dust.

The estimated dust parameters for M31 are compared with those derived using the independent maps in DA14.

We compare the DL optical extinction estimates with those of *Pl*-MBB. We further compare the DL model reddening estimates with near IR reddening estimates from quasi-stellar objects (hereafter QSOs) from the Sloan Digital Sky Survey (SDSS, York et al. 2000), and from stellar reddening maps in dark clouds obtained from the Two Micron All Sky Survey (2MASS, Skrutskie et al. 2006). These reveal significant discrepancies that call for a revision of the DL model. We find an empirical parameterization that renormalizes the current DL model and provides insight into what is being compensated for through the renormalization.

We use the DL model parameter U_min to bin the *Planck* and *IRAS* data for the diffuse ISM and compress the spectral information to a family of 20 dust SEDs, normalized per A_V, which

[1] *Planck* (`http://www.esa.int/Planck`) is a project of the European Space Agency (ESA) with instruments provided by two scientific consortia funded by ESA member states (in particular the lead countries France and Italy), with contributions from NASA (USA) and telescope reflectors provided by a collaboration between ESA and a scientific consortium led and funded by Denmark.

[2] From now on we will refer to the *WISE*, *IRAS*, and DIRBE bands as *WISE* 12, *IRAS* 60, *IRAS* 100, DIRBE 100, DIRBE 140, and DIRBE 240, by attaching the band reference wavelength (in μm) to the spacecraft or instrument name, and to the *Planck* bands as *Planck* 857, *Planck* 545, *Planck* 353, *Planck* 217, *Planck* 143, and *Planck* 100, by attaching the band reference frequency (in GHz) to the spacecraft name.

may be used to test and empirically calibrate dust models. We also provide the *Planck* 217 (1.38 mm) and *Planck* 143 (2.10 mm) photometric constraints, which are not used in the current dust modelling.

This paper is organized as follows. We describe the data sets in Sect. 2. In Sect. 3, we present the DL dust model, the model parametrization and the method we use to fit the model to the data. The model results are described in Sect. 4. We present the maps of the model parameters (Sect. 4.1), analyse the model ability to fit the data (Sect. 4.2) and assess the robustness of our determination of the dust mass surface density (Sect. 4.3). We compare the dust A_V estimates with the MBB all-sky modelling results from *Pl*-MBB in Sect. 5. In Sect. 6 we propose an empirical correction to the DL A_V estimates based on the comparison with QSO SDSS data. The DL model is used to compress the *Planck* and *IRAS* data into a family of 20 dust SEDs that account for the main variations of the dust emission properties in the diffuse ISM (Sect. 7). In Sect. 8, we extend our assessment of the DL A_V map to molecular clouds. The difference between A_V derived from the DL model and optical observations is related to dust emission properties and their evolution within the ISM in Sect. 9. We conclude in Sect. 10. The paper has four appendices. In Appendix A, we compare our analysis of *Planck* and *IRAS* observations of M31 with earlier DL modelling of *Herschel* and *Spitzer* data. In Appendix B, we detail how we estimate A_V towards QSOs observed with SDSS. In Appendix C, we analyse the impact of cosmic infrared background (CIB) anisotropies in our dust modelling. In Appendix D, we describe the data products made public in the *Planck* Legacy Archive.

2. Data sets

We use the full mission maps of the high frequency instrument of *Planck* that were made public in February 2015 (Planck Collaboration I 2016; Planck Collaboration VIII 2016). The zodiacal light has been estimated and removed from the maps (Planck Collaboration XIV 2014). We remove the cosmic microwave background, as estimated with the `SMICA` algorithm (Planck Collaboration IX 2016), from each *Planck* map. Following *Pl*-MBB we do not remove the CO(3-2) contribution to the *Planck* 353 GHz band[3].

A constant offset (listed in the column marked removed CIB monopole of Table 1) was added to the maps by the *Planck* team to account for the CIB in extragalactic studies, and we proceed to subtract it. Since the *Planck* team calibrated the zero-level of the Galactic emission before the zodiacal light was removed, an additional offset correction is necessary. To determine this (small) offset, we proceed exactly as in Sect. 5 of Planck Collaboration VIII (2014) by correlating the *Planck* 857 GHz map to the Leiden/Argentine/Bonn Survey of Galactic H I, and then cross-correlating each of the lower frequency *Planck* maps to the 857 GHz map, over the most diffuse areas at high Galactic latitude. These offsets make the intercepts of the linear regressions between the *Planck* and H I emission equal to zero emission for a zero H I column density. We note that we did not attempt to correct the *Planck* maps for a potential residual of the CMB dipole as done by *Pl*-MBB. This is not crucial for our study because we do not use microwave frequencies for fitting the DL model.

We complement the *Planck* maps with *IRAS* 60 and *IRAS* 100 maps. We employ the *IRAS* 100 map presented in *Pl*-MBB. It combines the small scale ($< 30'$) features of the map presented by the Improved reprocessing of the *IRAS* survey (IRIS, Miville-Deschênes & Lagache 2005), and the large scale ($> 30'$) features of the map presented by Schlegel et al. (1998, hereafter SFD). The zodiacal light emission has been estimated and removed from the SFD map, and therefore it is removed from the map we are employing[4]. We employ the *IRAS* 60 map presented by the IRIS team, with a custom estimation and removal of the zodiacal light[5]. The zero level of the *IRAS* maps is adjusted so it is consistent with the *Planck* 857 GHz map.

In Sects. 5 and 9.1, we compare our work with the MBB all-sky modelling results from *Pl*-MBB. To perform a consistent comparison, in these sections we use the same *Planck* and *IRAS* data as in *Pl*-MBB, i.e. the nominal mission *Planck* maps corrected for zodiacal light (Planck Collaboration I 2014) with the monopole and dipole corrections estimated by *Pl*-MBB.

WISE mapped the sky at 3.4, 4.6, 12, and 22 μm. Meisner & Finkbeiner (2014) presented a reprocessing of the entire *WISE* 12 μm imaging data set, generating a high resolution, full-sky map that is free of compact sources and was cleaned from several contaminating artefacts. The zodiacal light contribution was subtracted from the *WISE* map assuming that on spatial scales larger than 2° the dust emission at 12 μm is proportional to that in the Planck 857 GHz band. This effectively removes the zodiacal emission but at the cost of losing information on the ratio between *WISE* and *Planck* maps on scales larger than 2°. About 18 % of the *WISE* map is contaminated by the Moon or other solar system objects. Aniano (A15, private communication) prepared a new *WISE* map, with an improved correction of the contaminated area, which we use in this paper.

For typical lines of sight in the diffuse ISM, the dust SED peaks in the $\lambda = 100-160$ μm range. DIRBE produced low resolution (FWHM $= 42'$) all-sky maps at 140 and 240 μm, which can be used to test the robustness of our modelling. Additionally, we perform a lower resolution (1° FWHM) modelling, including the DIRBE 140 and DIRBE 240 photometric constraints. We use the DIRBE zodiacal light-subtracted mission average (ZSMA) maps. This modelling allows us to evaluate the importance of adding photometric constraints near the dust SED peak, which are absent in the *Planck* and *IRAS* data.

The FIS instrument (Kawada et al. 2007) on board the *AKARI* spacecraft (Murakami et al. 2007) observed the sky at four FIR bands in the $50-180$ μm range. Unfortunately, *AKARI* maps were made public (Doi et al. 2015) after this paper was submitted. Moreover, the way their mosaic tiles are chosen and significant mismatch of the zero level of the Galactic emission among the tiles prevent a straightforward integration of the *Akari* data into the present modeling.

All maps were convolved to yield a Gaussian PSF, with FWHM $= 5.'0$, slightly broader than all the native resolution of the *Planck* maps. We use the Hierarchical Equal Area iso-Latitude Pixelization (`HEALPix`) of a sphere coordinates (Górski et al. 2005)[6]. We work at resolution $N_{\rm side} = 2\,048$, so the maps

[3] The current CO maps are noisy in the low surface brightness areas, and therefore subtracting these small contributions increases the noise level significantly.

[4] The zodiacal light emission contributes mainly at scales larger than $30'$, therefore, its contribution is subtracted when we retain the large scales of the SDF map.

[5] The new IRIS data reduction and a description are available at `http://www.cita.utoronto.ca/~mamd/IRIS/IrisOverview.html`

[6] A full description of `HEALPix` and its software library can be found at `http://healpix.jpl.nasa.gov`.

Table 1. Description of the data used.

Band	λ^a [μm]	FWHM[b] [arcmin]	Calibration Uncertainty[c] [%]	CIB anisotropies[d] [MJy sr^{-1}]	Removed CIB monopole [MJy sr^{-1}]	Removed offset [MJy sr^{-1}]
Planck 100 GHz[e]	3000	9.68	0.09		0.0030	-0.000240
Planck 143 GHz[e]	2098	7.30	0.07		0.0079	0.000694
Planck 217 GHz[e]	1283	5.02	0.16		0.033	-0.0032
Planck 353 GHz	850	4.94	0.78	0.016	0.13	-0.007616
Planck 545 GHz	550	4.83	6.1	0.044	0.35	0.0004581
Planck 857 GHz	350	4.64	6.4	0.010	0.64	-0.04284
DIRBE 240 μm	248	42.0	11.6			0.975961
DIRBE 140 μm	148	42.0	10.6			1.16576
DIRBE 100 μm	100	42.0	13.6			0.87963
IRAS 100 μm	100	4.3	13.5	0.010		-0.06381
IRAS 60 μm	60	4.0	10.4			0.112
WISE 12 μm	12	0.25	10.0			0.0063

a Central wavelength of the spectral band.
b Angular resolution (FWHM) of the original map.
c Assumed calibration uncertainty as a percentage of the image intensity.
d Root mean square (rms) of the CIB anisotropies in the band at 5′ resolution.
e *Planck* 217, *Planck* 143, *Planck* 100 and DIRBE bands are not used to constraint the current dust model.

have a total of $12 \times 2\,048 \times 2\,048 = 50\,331\,648$ pixels. Each pixel is a quadrilateral of area 2.94 arcmin^2 (i.e. about 1.′7 on a side). All maps and results presented in the current paper are performed using this resolution, except those of Sects.4.3.2 and 7. The most relevant information on the data sets that are used is presented in Table 1. The amplitudes of the CIB anisotropies (CIBA) depend on the angular scale; the values listed in Table 1 are for the 5′ resolution of our data modelling.

3. The DL model

The DL dust model is a physical approach to modelling dust. It assumes that the dust consists of a mixture of amorphous silicate grains and carbonaceous grains heated by a distribution of starlight intensities. We employ the Milky Way grain size distributions (Weingartner & Draine 2001), chosen to reproduce the wavelength dependence of the average interstellar extinction within the solar neighbourhood. The silicate and carbonaceous content of the dust grains has been constrained by observations of the gas phase depletions in the ISM. The carbonaceous grains are assumed to have the properties of PAH molecules or clusters when the number of carbon atoms per grain $N_C \lesssim 10^5$, but to have the properties of graphite when $N_C \gg 10^5$. DL describes the detailed computation of the model SED, and AD12 describes its use in modelling resolved dust emission regims.

3.1. Parameterization

The IR emission of the DL dust model is parametrized by six parameters, Σ_{M_d}, q_{PAH}, U_{min}, U_{max}, α, and γ. The definition of these parameters is now reviewed. The model IR emission is proportional to the dust mass surface density Σ_{M_d}. The PAH abundance is measured by the parameter q_{PAH}, defined to be the fraction of the total grain mass contributed by PAHs containing $N_C < 10^3$ C atoms[7]. As a result of single-photon heating, the tiny PAHs contributing to q_{PAH} radiate primarily at $\lambda < 30\,\mu$m, and this fraction is constrained by the *WISE* 12 band. Weingartner & Draine (2001) computed different grain size distributions for dust grains in the diffuse ISM of the MW, which are used in DL. The models in this MW3.1 series are all consistent with the average interstellar extinction law[8], but have different PAH abundances in the range $0.0047 \leq q_{PAH} \leq 0.047$. Draine et al. (2007) found that the SINGS galaxies span the full range of q_{PAH} models computed, with a median value of $q_{PAH} = 0.034$. Models are further extrapolated into a (uniformly sampled) q_{PAH} grid, using $\delta q_{PAH} = 0.001$ intervals in the range $0 \leq q_{PAH} \leq 0.10$, as described by AD12.

Each dust grain is assumed to be heated by radiation with an energy density per unit frequency

$$u_\nu = U \times u_\nu^{MMP83}, \quad (1)$$

where U is a dimensionless scaling factor and u_ν^{MMP83} is the ISRF estimated by Mathis et al. (1983) for the solar neighbourhood. A fraction $(1 - \gamma)$ of the dust mass is assumed to be heated by starlight with a single intensity $U = U_{min}$, and the remaining fraction γ of the dust mass is exposed to a power-law distribution of starlight intensities between U_{min} and U_{max}, with $dM/dU \propto U^{-\alpha}$. From now on, we call these the diffuse cloud and photodissociation regions (PDR) components respectively. AD12 found that the observed SEDs in the NGC 628 and NGC 6946 galaxies are consistent with DL models with $U_{max} = 10^7$. Given the limited number of photometric constraints, we fix the values of $U_{max} = 10^7$ and $\alpha = 2$ to typical values found in AD12. The DL models presented in DL07 are further interpolated into a (finely sampled) U_{min} grid using $\delta U_{min} = 0.01$ intervals, as described by A15.

Therefore, in the present work the DL parameter grid has only four dimensions, Σ_{M_d}, q_{PAH}, U_{min}, and γ. We explore the ranges $0.00 \leq q_{PAH} \leq 0.10$, $0.01 \leq U_{min} \leq 30$, and $0 \leq \gamma \leq 1.0$. For this range of parameters, we build a DL model library that contains the model SED in a finely-spaced wavelength grid for $1\,\mu\text{m} < \lambda < 1\text{cm}$.

[7] For the size distribution in the DL models, the mass fraction contributed by PAH particles containing $N_C < 10^6$ C atoms is 1.478 q_{PAH}.

[8] In the details of their size distributions and dust composition (e.g. the lack of ices), these models will not be as appropriate for dust in dark molecular clouds.

As a derived parameter, we define the ratio

$$f_{\rm PDR} \equiv \frac{L_{\rm PDR}}{L_{\rm dust}}\,, \tag{2}$$

where $L_{\rm PDR}$ is the luminosity radiated by dust in regions where $U > 10^2$ and $L_{\rm dust}$ is the total power radiated by the dust. Clearly, $f_{\rm PDR}$ depends on the fitting parameter γ in the numerator and, through the denominator, also depends on $U_{\rm min}$. Dust heated with $U > 10^2$ emits predominantly in the $\lambda < 100\,\mu$m range; therefore, the *IRAS* 60 to *IRAS* 100 intensity ratio can be increased to very high values by taking $f_{\rm PDR} \rightarrow 1$. Conversely, for a given $U_{\rm min}$, the minimum *IRAS* 60/*IRAS* 100 intensity ratio corresponds to models with $f_{\rm PDR} = 0$.

Another derived quantity, the mass-weighted mean starlight heating intensity $\langle U \rangle$, for $\alpha = 2$, is given by

$$\langle U \rangle = (1-\gamma)\,U_{\rm min} + \gamma\,U_{\rm min}\,\frac{\ln(U_{\rm max}/U_{\rm min})}{1-U_{\rm min}/U_{\rm max}}. \tag{3}$$

Adopting the updated carbonaceous and astrosilicate densities recommended by DA14, the DL model used here is consistent with the MW ratio of visual extinction to H column density, $A_V/N_{\rm H} = 5.34\times10^{-22}$ mag cm^2 (i.e. $N_{\rm H}/E(B-V) = 5.8\times10^{21}$ cm^{-2} mag^{-1}, Bohlin et al. 1978), for a dust to H mass ratio $\Sigma_{M_{\rm d}}/N_{\rm H}m_{\rm H} = 0.0091$. From the dust surface density, we infer the model estimate of the visual extinction

$$A_{\rm V,DL} = 0.74\left(\frac{\Sigma_{M_{\rm d}}}{10^5{\rm M}_\odot\,{\rm kpc}^{-2}}\right){\rm mag}\,. \tag{4}$$

3.2. Fitting strategy and implementation

For each individual pixel, we find the DL parameters $\{\Sigma_{M_{\rm d}},\, q_{\rm PAH},\, U_{\rm min},\, \gamma\}$ that minimize

$$\chi^2 \equiv \sum_k \frac{[S_{\rm obs}(\lambda_k) - S_{\rm DL}(\lambda_k)]^2}{\sigma^2_{\lambda_k}}\,, \tag{5}$$

where $S_{\rm obs}(\lambda_k)$ is the observed flux density per pixel, $S_{\rm DL}(\lambda_k)$ is the DL emission SED convolved with the response function of the spectral band k, and σ_{λ_k} is the $1\,\sigma$ uncertainty in the measured intensity density at wavelength λ_k. We use a strategy similar to that of AD12 and define σ_{λ_k} as a sum in quadrature of five uncertainty sources:

- the calibration uncertainty (proportional to the observed intensity);
- the zero-level (offset) uncertainty;
- the residual dipole uncertainty;
- CIB anisotropies;
- the instrumental noise.

Values for these uncertainties (except the noise) are given in Table 1. To produce the best-fit parameter estimates, we fit the DL model to each pixel independently of the others.

We observe that for a given set of parameters $\{q_{\rm PAH},\, U_{\rm min}\}$, the model emission is bi-linear in $\{\Sigma_{M_{\rm d}},\, \gamma\}$. This allows us to easily calculate the best-fit values of $\{\Sigma_{M_{\rm d}},\, \gamma\}$ for a given parameter set $\{q_{\rm PAH},\, U_{\rm min}\}$. Therefore, when looking for the best-fit model in the full four-dimensional model parameter space $\{\Sigma_{M_{\rm d}},\, q_{\rm PAH},\, U_{\rm min},\, \gamma\}$, we only need to perform a search over the two-dimensional subspace spanned by $\{q_{\rm PAH},\, U_{\rm min}\}$. The DL model emission convolved with the instrumental bandpasses, $S_{\rm DL}(\lambda_k)$, was pre-computed for a $\{q_{\rm PAH},\, U_{\rm min}\}$ parameter grid, allowing the multi-dimensional search for optimal parameters to be performed quickly by brute force, without relying on non-linear minimization algorithms.

In order to determine the uncertainties on the estimated parameters in each pixel, we proceed as follows: we simulate 100 observations by adding noise to the observed data; we fit each simulated SED using the same fitting technique as for the observed SED; and we study the statistics of the fitted parameters for the various realizations. The noise added in each pixel is a sum of the five contributions listed in the previous paragraph, each one assumed to be Gaussian distributed. We follow a strategy similar to that of AD12, taking a pixel-to-pixel independent contribution for the data noise and correlated contributions across the different pixels for the other four sources of uncertainty. For simplicity, we assume that none of the uncertainties are correlated across the bands. The parameter error estimate at a given pixel is the standard deviation of the parameter values obtained for the simulated SEDs. For typical pixels, the uncertainty on the estimated parameters is a few percent of their values (e.g. Figure 2 shows the signal-to-noise (S/N) ratio of $\Sigma_{M_{\rm d}}$).

4. Dust modelling results and fitting robustness analysis

We present the results of the model fits (Sect. 4.1) and residual maps that quantify the model ability to fit the data (Sect. 4.2). In Sect. 4.1, we assess the robustness of the dust mass surface density with respect to the choice of frequency channels used in the fit.

4.1. Parameter maps

Figure 1 shows the all-sky maps of the fitted dust parameters. The left column corresponds to a Mollweide projection of the sky in Galactic coordinates, and the centre and right columns correspond to orthographic projections of the southern and northern hemispheres, centred on the corresponding Galactic poles. The top row corresponds to the dust mass surface density, $\Sigma_{M_{\rm d}}$, the main output of the model on which we focus our analysis in the next sections of the paper. Away from the Galactic plane, this map displays the structure of molecular clouds and the diffuse ISM in the solar neighbourhood. The middle row shows the map of $U_{\rm min}$ computed at the $5'$ resolution of the IRAS and Planck data. At high Galactic latitude, the CIB anisotropies induce a significant scatter in $U_{\rm min}$. Extragalactic point sources also contribute to the scatter of $U_{\rm min}$ where the Galactic dust emission is low. At low Galactic latitudes, the $U_{\rm min}$ values tend to be high ($U_{\rm min} > 1$) in the inner Galactic disk and low ($U_{\rm min} < 1$) in the outer galactic disk. The $U_{\rm min}$ map present structures aligned with the ecliptic plane, especially at high Galactic and low ecliptic latitudes, which are likely to be artefacts reflecting uncertainties in the subtraction of the zodiacal emission.

The $f_{\rm PDR}$ map shows artefact structures aligned with the ecliptic plane especially at high Galactic and low ecliptic latitudes. These artefacts are likely to be caused by residual zodiacal light in the *IRAS* 60 maps. As shown in Section 4.3.1, the dust mass estimates are not strongly biased in these regions. Figure 1 does not display the $q_{\rm PAH}$ maps, which are presented by A15 together with the corrected *WISE* data. The mass fraction in the PAH grains is relatively small, and therefore, variations in $q_{\rm PAH}$ do not have a major impact on the $\Sigma_{M_{\rm d}}$. If instead of using the *WISE* data to constrain $q_{\rm PAH}$, we simply fix $q_{\rm PAH} = 0.04$, the $\Sigma_{M_{\rm d}}$ estimates will only change by a few percent.

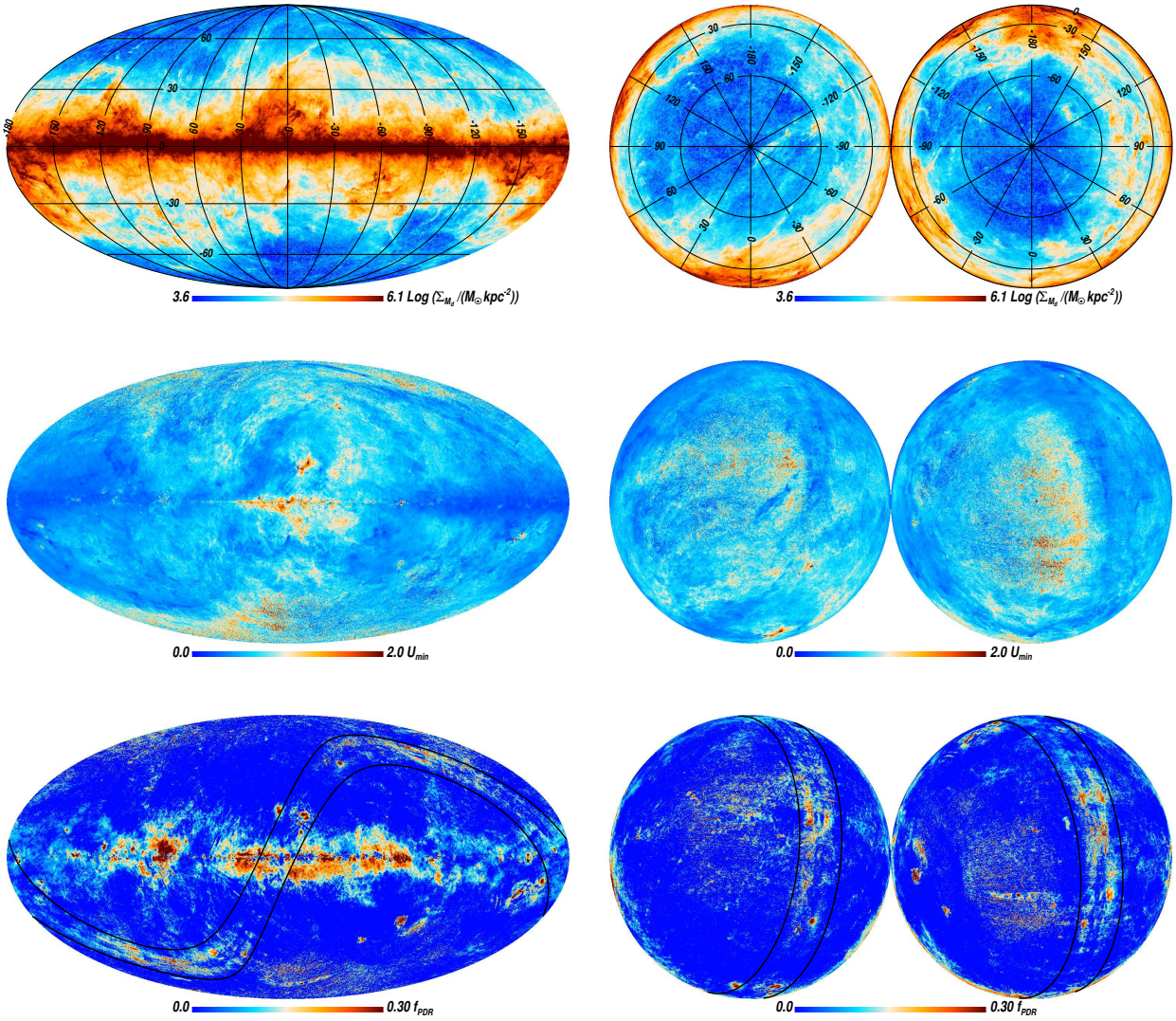

Fig. 1. DL fitted parameter maps. The top row corresponds to the dust mass surface density, Σ_{M_d}, the middle row to the starlight intensity heating the bulk of the dust, U_min, and the bottom row to the fraction of dust luminosity emitted by dust heated with high stellar intensities, f_PDR. The left column corresponds to a Mollweide projection of the sky in Galactic coordinates, and the centre and right columns correspond to orthographic projections of the southern and northern hemispheres centred on the corresponding Galactic poles. A Galactic coordinate grid is plotted in the maps of the first row. Lines of ecliptic latitude at ±10° are plotted in the maps of the bottom row.

Figure 2 shows a map of the dust emitted luminosity surface density, Σ_{L_d}, the mean intensity heating the dust, $\langle U \rangle$, the χ^2 per degree of freedom (dof) of the fit, χ^2/Ndof, and a map of the S/N ratio of the dust mass surface density Σ_{M_d}.

The χ^2/Ndof map scatter around unity in the high Galactic latitude areas, where the data uncertainties are noise-dominated. The χ^2/Ndof is slightly larger than 1 in the inner Galactic disk and several other localized areas. In the outer Galactic disk the χ^2/Ndof is smaller than 1, presumably due to overestimation of the uncertainties. Over much of the sky, the fit to the FIR SED is not as good as in *Pl*-MBB; the MBB fit has three fitting parameters in contrast with the DL model which has only two, Σ_{M_d} and U_min[9].

4.2. Dust model photometric performance: residual maps

As shown in the χ^2/Ndof map in Figure 2, the DL model fits the observed SED satisfactorily (within 1 σ) over most of the sky areas. However, the model SEDs have systematic departures from the observed SED in the inner Galactic disk, at low ecliptic latitude, and in localized regions. We note that the spectral index of the dust FIR–submm opacity is fixed in the DL model; it cannot be adjusted to match the observed SED closely. This is why MBB spectra (with one extra effective degree of freedom) fits the observed SED better in some regions. The departures of the model in the low ecliptic latitude regions could be caused by defects in the zodiacal light estimation (and removal) from the photometric maps that the model cannot accommodate. In the Magellanic Clouds (MC) the DL model fails to fit the data[10]. The MC exhibit surprisingly strong emission at submm and millimetre wavelengths. Planck Collaboration XVII (2011)

[9] The q_PAH parameter does not affect significantly the FIR SED; it only affects significantly the *WISE* 12 photometry. The f_PDR parameter affect mostly IRAC 60 photometry, without contributing significantly to the remaining FIR bands.

[10] The MC appear as two red spots in the southern hemisphere in the top row of Figure 4

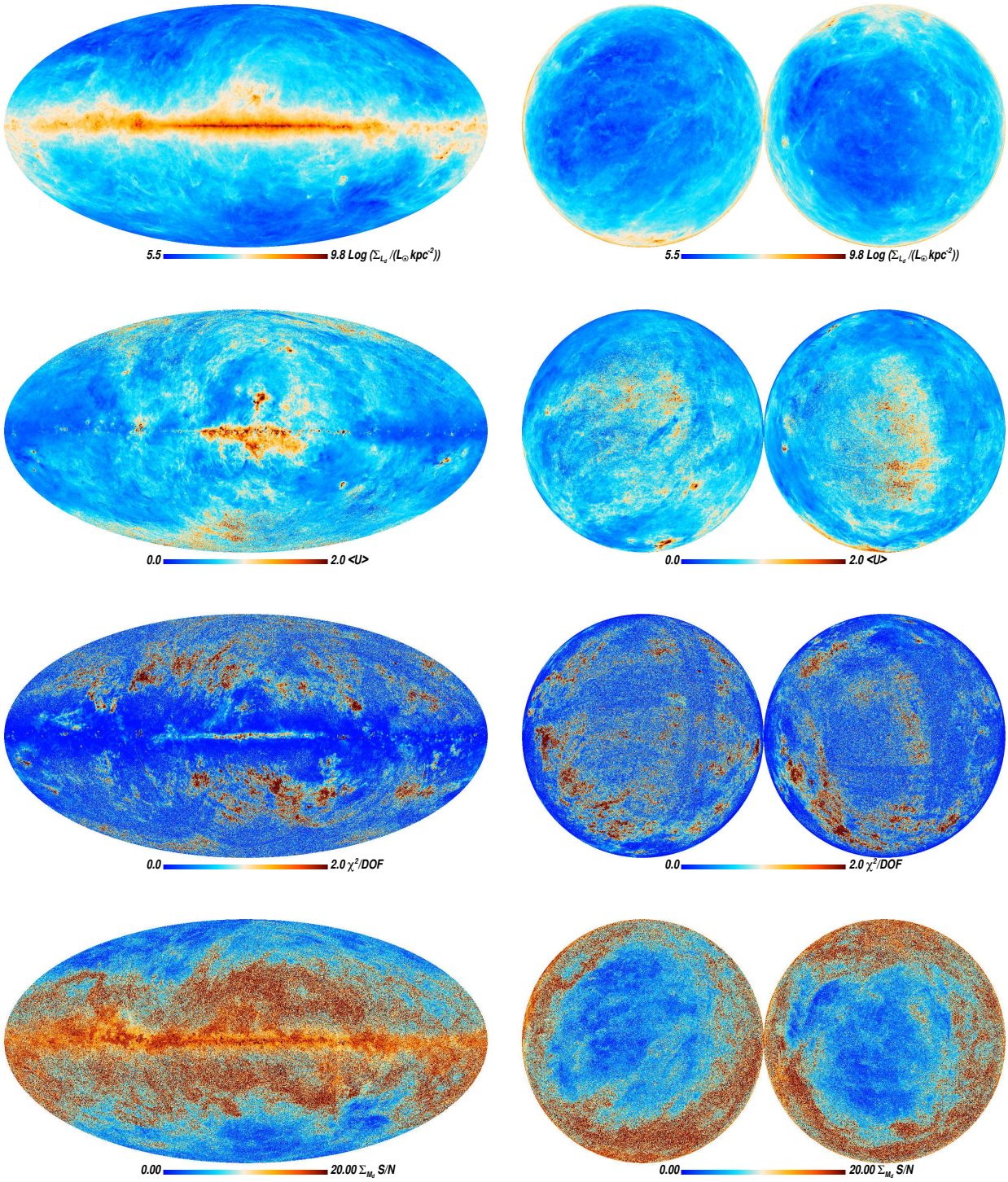

Fig. 2. DL derived parameters. The top row corresponds to the dust luminosity surface density, Σ_{L_d}, the second row shows the mean intensity heating the dust, $\langle U \rangle$, the third row shows the χ^2 per degree of freedom of the fit, χ^2/Ndof, and the bottom row the S/N map of the dust mass surface density Σ_{M_d}.

conclude that conventional dust models cannot account for the observed 600 − 3 000 μm emission without invoking unphysically large amounts of very cold dust. Draine & Hensley (2012) suggest that magnetic dipole emission from magnetic grain materials could account for the unusually strong submm emission from the Small MC.

Figures 3 and 4 show the model departures from the photometric constraints used in the fits. Each panel shows the difference between the model predicted intensity and the observed intensity, divided by the observed uncertainty. The systematic departures show that the physical model being used does not have sufficient parameters or flexibility to fit the data perfectly.

By increasing γ (i.e. the PDR component), the DL model can increase the *IRAS* 60 to *IRAS* 100 ratio to high values, without contributing much to the *Planck* intensities. Thus, in principle, the model should never underpredict the *IRAS* 60

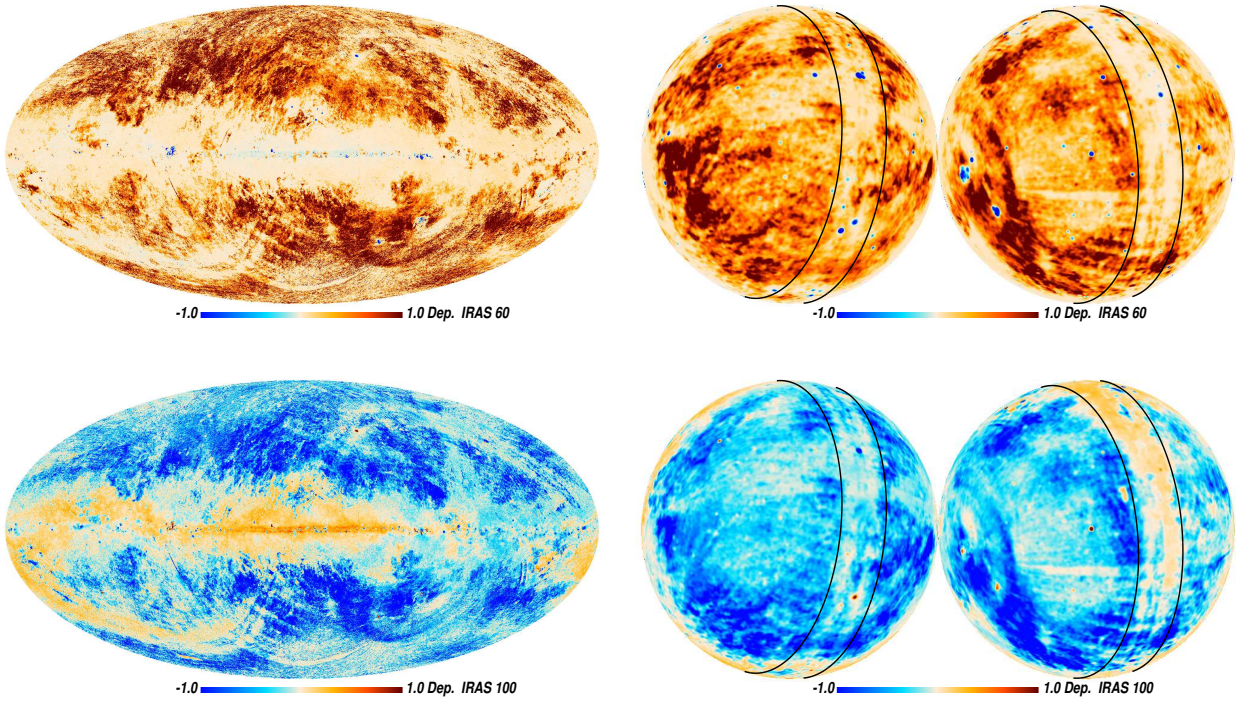

Fig. 3. Comparison between the model and the *IRAS* data used to constrain the fit. Each panel shows the model departure from the data defined as Dep. = (Model − Map)/Uncertainty. The top row corresponds to *IRAS* 60, and the bottom row to *IRAS* 100. The polar projection maps are smoothed to 1° resolution to highlight the systematic departures, and lines of Ecliptic latitude at ±10° are added for reference.

emission. Figure 3 shows the model performance for fitting the *IRAS* bands; several high latitude areas (mostly with $f_{\rm PDR} = 0$) have *IRAS* 60 overpredicted and *IRAS* 100 underpredicted. Both model components (the diffuse cloud and PDR components) have an *IRAS* 60 / *IRAS* 100 intensity ratio slightly larger than the ratio observed in these regions. There are several areas where the *IRAS* 60 / *IRAS* 100 ratio is below the value for the best-fit $U_{\rm min}$, hence in these areas the model (with $f_{\rm PDR} = 0$) overpredicts *IRAS* 60. This systematic effect is at the $1-2\,\sigma$ level (i.e. $10-20\,\%$).

In the inner Galactic disk the DL model tends to underpredict the $350\,\mu$m and overpredict the $850\,\mu$m emission (see Figure 4). The observed SED is systematically steeper than the DL SED in the $350-850\,\mu$m range (i.e. between *Planck* 857 and *Planck* 353). Similar results were found in the central kiloparsec of M31 in the $250-500\,\mu$m range (DA14). The MBB fit of these regions, presented in *Pl*-MBB, finds larger values of the opacity spectral index β ($\beta \approx 2.2$) than the typical value found in the low-and mid-range dust surface density areas ($\beta \approx 1.65$). The DL SED peak can be broadened by increasing the PDR component (i.e. by raising γ or $f_{\rm PDR}$), but it cannot be made steeper than the $\gamma = 0$ ($f_{\rm PDR} = 0$) models, and the model therefore fails to fit the $350-850\,\mu$m SED in these regions.

Following DA14, we define

$$\Upsilon_{\rm DL} = \frac{\log(\kappa_{\rm DL} * F857/\kappa_{\rm DL} * F353)}{\log(857{\rm GHz}/353{\rm GHz})}, \qquad (6)$$

as the effective power-law index of the DL dust opacity between $350\,\mu$m and $850\,\mu$m, where $\kappa_{\rm DL} * F$ is the assumed absorption cross-section per unit dust mass convolved with the respective *Planck* filter. For the DL model[11] this ratio is $\Upsilon_{\rm DL} \approx 1.8$.

[11] If the *Planck* filters were monochromatic at the nominal frequencies, then $\Upsilon_{\rm DL} = 1.82$ (see Table 2 in DA14). For the real *Planck* filters the $\Upsilon_{\rm DL}$ value is a constant close to 1.8.

If the dust temperatures in the fitted DL model were left unchanged, then the predicted *Planck* 857/*Planck* 353 intensity ratio could be brought into agreement with observations if $\Upsilon_{\rm DL}$ were changed by $\delta\Upsilon$ given by

$$\delta\Upsilon = \log \frac{I_\nu(Planck\ 857)/I_\nu(Planck\ 353)}{I_\nu({\rm DL}\ 857)/I_\nu({\rm DL}\ 353)} / \log \frac{857{\rm GHz}}{353{\rm GHz}}, \qquad (7)$$

where we denote $I_\nu(Planck\ ...)$ the observed *Planck* intensity, and $I_\nu({\rm DL}\ ...)$ the corresponding intensity for the DL model.

Figure 5 shows the $\delta\Upsilon$ map, i.e. the correction to the spectral index of the submm dust opacity that would bring the DL SED into agreement with the observed SED if the dust temperature distribution is left unchanged. The observed SED is steeper than the DL model in the inner Galactic disk ($\delta\Upsilon_{\rm DL} \approx 0.3$) and shallower in the MC ($\delta\Upsilon_{\rm DL} \approx -0.3$). The correction to the spectral index $\delta\Upsilon$ is positive on average. The average value of $\delta\Upsilon$ tends to increase with $\Sigma_{M_{\rm d}}$, but the scatter of the individual pixels is always larger than the mean. The large dispersion in the low surface brightness areas is mainly due to CIB anisotropies. The dispersion in bright sky areas, e.g. along the Galactic plane and in molecular clouds off the plane, may be an indicator of dust evolution, i.e. variations in the FIR emission properties of the dust grains in the diffuse ISM.

Modifying the spectral index of the dust opacity in the model would change $U_{\rm min}$ and thereby the dust mass surface density. The $\delta\Upsilon$ map should be regarded as a guide on how to modify the dust opacity in future dust models, rather than as the exact correction to be applied to the opacity law per se.

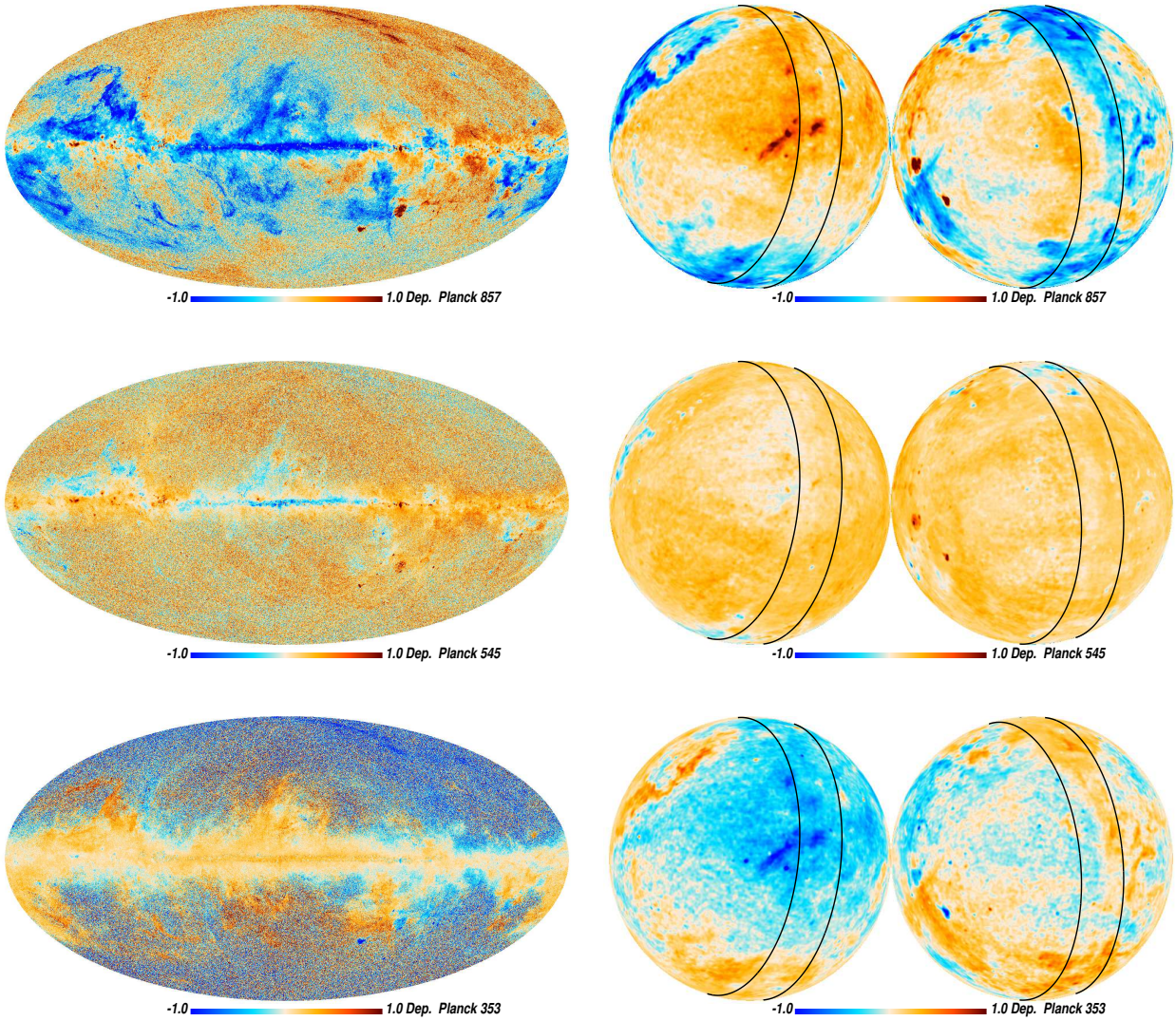

Fig. 4. Comparison between the model and the *Planck* data used to constrain the fit. Each panel shows the model departure from the data defined as Dep. = (Model - Map)/Uncertainty. The top row corresponds to *Planck* 857, the central row to *Planck* 545, and the bottom row to *Planck* 353. The polar projection maps are smoothed to 1° resolution to highlight the systematic departures, and lines of Ecliptic latitude at ±10° are added for reference.

4.3. Robustness of the mass estimate

4.3.1. Importance of *IRAS* 60

To study the potential bias introduced by *IRAS* 60, due to residuals of zodiacal light estimation (whose relative contribution is the largest in the *IRAS* 60 band) or the inability of the DL model to reproduce the correct SED in this range, one can perform modelling without the *IRAS* 60 constraint. In this case we set $\gamma = 0$, i.e. we allow only the diffuse cloud component ($f_{\rm PDR} = 0$), and so we have a two-parameter model.

Figure 6 shows the ratio of the dust mass estimated without using the *IRAS* 60 constraint and with $\gamma = 0$ to that estimated using *IRAS* 60 and allowing γ to be fitted (i.e. our original modelling). The left panel shows all the sky pixels and the right panel only the pixels with $f_{\rm PDR} > 0$. In the mid-and-high-range surface mass density areas ($\Sigma_{M_{\rm d}} > 10^5 {\rm M}_\odot\,{\rm kpc}^{-2}$), where the photometry has good S/N, both models agree well, with a rms scatter below 5 %. The inclusion or exclusion of the *IRAS* 60 constraint does not significantly affect our dust mass estimates in these regions. In the low surface density areas, inclusion of the *IRAS* 60 does not change the $\Sigma_{M_{\rm d}}$ estimate in the $f_{\rm PDR} > 0$ areas, but it leads to an increase of the $\Sigma_{M_{\rm d}}$ estimate in the $f_{\rm PDR} = 0$ pixels. In the $f_{\rm PDR} = 0$ areas, the model can overpredict *IRAS* 60 in some pixels, and therefore, when this constraint is removed, the dust can be fitted with a larger $U_{\rm min}$ value reducing the $\Sigma_{M_{\rm d}}$ needed to reproduce the remaining photometric constraints. In the $f_{\rm PDR} > 0$ areas, the PDR component has a small contribution to the longer wavelengths constraints, and therefore removing the *IRAS* 60 constraint and PDR component has little effect in the $\Sigma_{M_{\rm d}}$ estimates.

4.3.2. Dependence of the mass estimate on the photometric constraints

The *Planck* and *IRAS* data do not provide photometric constraints in the $120\,\mu{\rm m} < \lambda < 300\,\mu{\rm m}$ range. This is a potentially problematic situation, since the dust SED typically peaks in this wavelength range. We can add the DIRBE 140 and DIRBE 240 constraints in a low resolution (FWHM $>$ 42′) modelling to test this possibility.

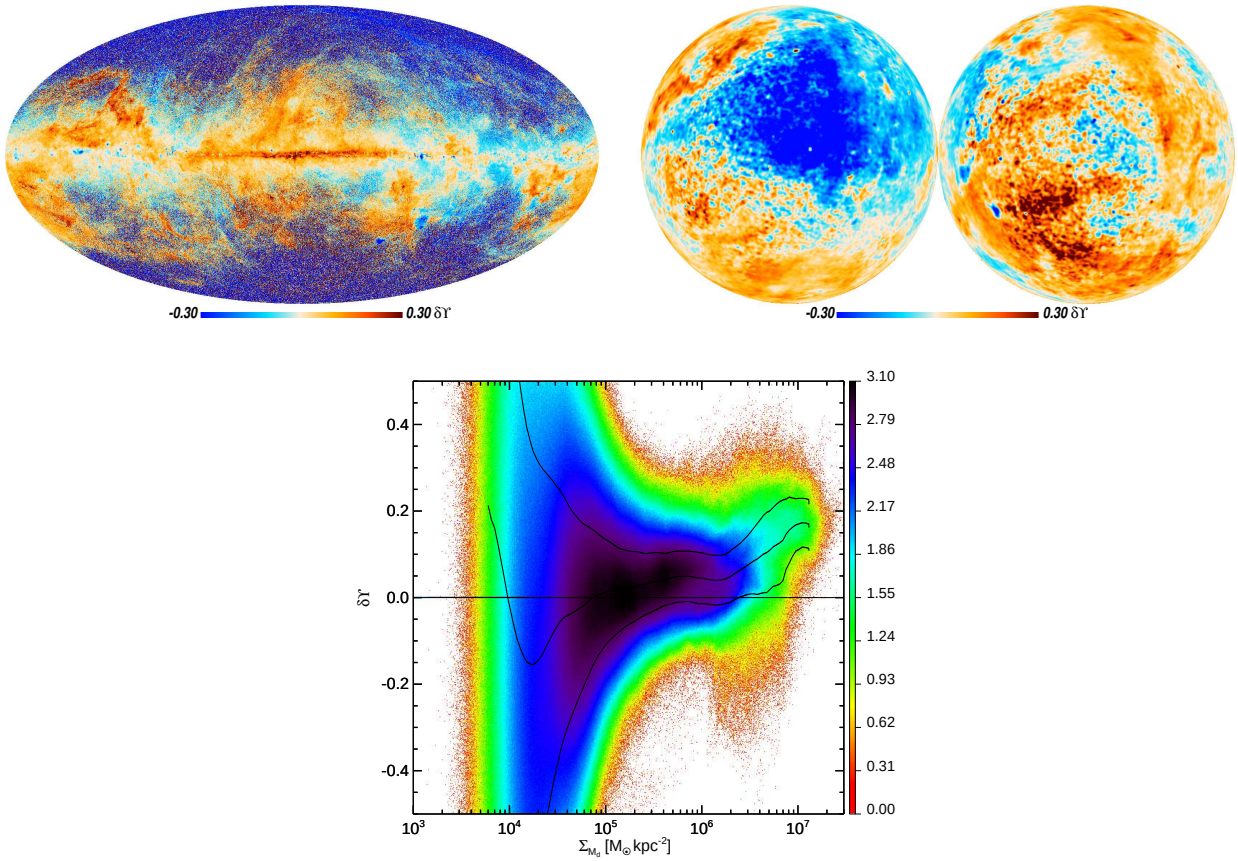

Fig. 5. Correction to the FIR opacity power law-index ($\delta\Upsilon$) needed to bring the DL SED into agreement with the *Planck* observations. The polar projection maps are smoothed to 1° resolution to highlight the systematic departures. The bottom row shows the scatter of the $\delta\Upsilon$ map as a function of Σ_{M_d}. Colour corresponds to the logarithm of the density of points, i.e. the logarithm of number of sky pixels that have a given (Σ_{M_d}, $\delta\Upsilon$) value in the plot. The curves correspond to the mean value and the $\pm 1\,\sigma$ dispersion.

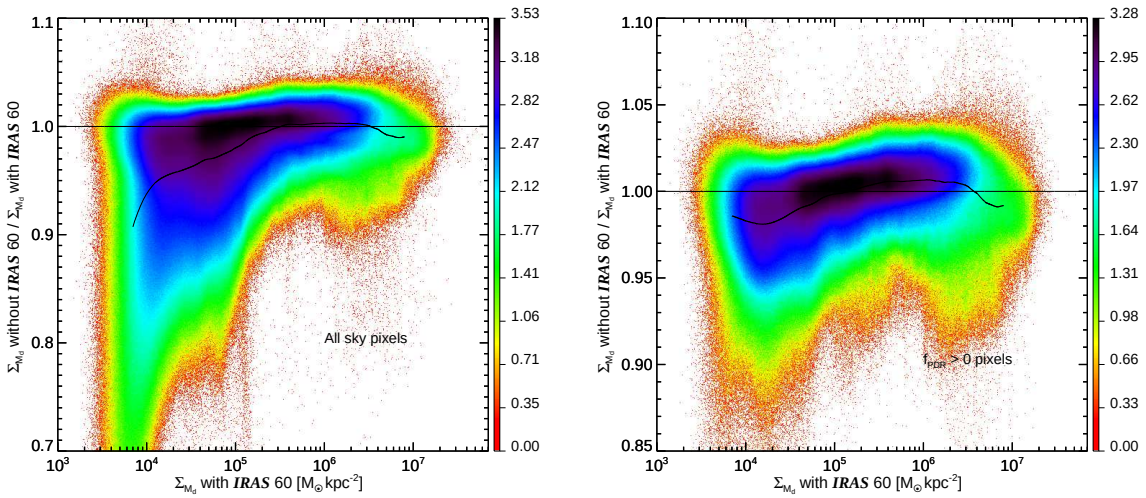

Fig. 6. Comparison between the dust mass estimates when the *IRAS* 60 constraint is excluded or included in the fit. The left panel shows all the sky pixels, and the right panel only the $f_{\rm PDR} > 0$ pixels. The vertical axis corresponds to the ratio of the inferred mass density of a fit without using the *IRAS* 60 constraint to that obtained when this constraint is present (see text). Colour corresponds to the logarithm of the density of points (see Fig. 5). The curve corresponds to the mean value.

We compare two analyses performed using a 1° FWHM Gaussian PSF. The first uses the same photometric constraints as the high resolution modelling (*WISE*, *IRAS*, and *Planck*), and the second additionally uses the DIRBE 140 and DIRBE 240 constraints. The results are shown in Figure 7. Both model fits agree very well, with differences between the dust mass estimates of only a few percent. Therefore, our dust mass estimates are not substantially affected by the lack of photometric constraints near

the SED peak. This is in agreement with similar tests carried out in *Pl*-MBB.

4.3.3. Validation on M31

In Appendix A we compare our dust mass estimates in the Andromeda galaxy (M31) with estimates based on an independent data set and processing pipelines. Both analyses use the DL model. This comparison allows us to analyse the impact of the photometric data used in the dust modelling. We conclude that the model results are not sensitive to the specific data sets used to constrain the FIR dust emission, validating the present modelling pipeline and methodology.

5. Comparison between the DL and MBB optical exctinction estimates

We now compare the DL optical extinction estimates with those from the MBB dust modelling presented in *Pl*-MBB, denoted $A_{V,\mathrm{DL}}$ and $A_{V,\mathrm{MBB}}$ respectively. We perform a DL dust modeling of the same *Planck* data as in *Pl*-MBB (i.e. the nominal mission maps)[12], the same *IRAS* 100 data, but our DL modelling also includes *IRAS* 60 and *WISE* 12 constraints. The DL model has two extra parameters (γ and q_{PAH}) that can adjust the *IRAS* 60 and *WISE* 12 intensity fairly independently of the remaining bands. Therefore, the relevant data that both models are using in determining the FIR emission are essentially the same. The MBB extinction map has been calibrated with external (optical) observational data, and so this comparison allows us to test the DL modelling against those independent data.

Pl-MBB estimated the optical extinction[13] $A_{V,\mathrm{QSO}}$ for a sample of QSOs from the SDSS survey. A single normalization factor Π was chosen to convert their optical depth τ_{353} map (the parameter of the MBB that scales linearly with the total dust emission, similar to the DL Σ_{M_d}) into an optical extinction map: $A_{V,\mathrm{MBB}} \equiv \Pi\,\tau_{353}$.

DL is a physical dust model and therefore fitting the observed FIR emission directly provides an optical extinction estimate, without the need for an extra calibration. However, if the DL dust model employs incorrect physical assumptions (e.g. the value of the FIR opacity), it may systematically over or under estimate the optical extinction corresponding to observed FIR emission.

Figure 8 shows the ratio of the DL and MBB A_V estimates. The top row shows the ratio map. The bottom row shows its scatter and histogram. Over most of the sky ($0.1\,\mathrm{mag} < A_{V,\mathrm{DL}} < 20\,\mathrm{mag}$), the $A_{V,\mathrm{DL}}$ values are larger than the $A_{V,\mathrm{MBB}}$ by a factor of 2.40 ± 0.40. This discrepancy is roughly independent of $A_{V,\mathrm{DL}}$. The situation changes in the very dense areas (inner Galactic disk). In these areas ($A_{V,\mathrm{DL}} \approx 100\,\mathrm{mag}$), the $A_{V,\mathrm{DL}}$ are larger than the $A_{V,\mathrm{MBB}}$ estimates by 1.95 ± 0.10.

In the diffuse areas ($A_{V,\mathrm{DL}} \lesssim 1$), where the $A_{V,\mathrm{MBB}}$ has been calibrated using the QSOs, $A_{V,\mathrm{DL}}$ overestimates $A_{V,\mathrm{MBB}}$, and therefore $A_{V,\mathrm{DL}}$ should overestimate $A_{V,\mathrm{QSO}}$ by a similar factor. This mismatch arises from two factors. (1) The DL dust physical parameters were chosen so that the model reproduces the SED proposed by Finkbeiner et al. (1999), based on FIRAS observations. It was tailored to fit the high latitude $I_\nu/N(\mathrm{H\,I})$ with $U_{\mathrm{min}} \approx 1$. The high latitude SED from *Planck* observations differs from that derived from FIRAS observations. The difference depends on the frequency and can be as high as 20 % (Planck Collaboration VIII 2014). The best fit to the mean *Planck* + *IRAS* SED on the QSO lines of sight is obtained for $U_{\mathrm{min}} \approx 0.66$. The dust total emission (luminosity) computed for the *Planck* and for the Finkbeiner et al. (1999) SED are similar. The dust total emission per unit of optical reddening (or mass) scales linearly with U_{min}. Therefore, we need $1/0.66 \approx 1.5$ more dust mass to reproduce the observed luminosity. This is in agreement with the results of Planck Collaboration Int. XVII (2014) who have used the dust - H I correlation at high Galactic latitudes to measure the dust SED per unit of H I column density. They find that their SED is well fit by the DL model for $U_{\mathrm{min}} = 0.7$ after scaling by a factor 1.45. (2) The optical extinction per gas column density used to construct the DL model is that of Bohlin et al. (1978). Recent observations show that this ratio needs to be decreased by a factor of approximately 1/1.4 (Liszt 2014a,b). Combining the two factors, we expect the $A_{V,\mathrm{DL}}$ to overestimate the $A_{V,\mathrm{QSO}}$ by about a factor of 2.

[12] The $A_{V,\mathrm{DL}}$ estimates based on the full mission *Planck* maps (the maps used in the remaining sections of this paper), and the nominal mission *Planck* maps differ by only a few percent over most of the sky.

[13] *Pl*-MBB actually determine optical reddening $E(B-V)$ for the QSO sample. Since a fixed extinction curve with $R_V = 3.1$ (see App. B.2) was used, this is equivalent to determining the optical extinction A_V.

6. Renormalization of the model extinction map

We proceed in our analysis of the model results characterizing how the ratio between the optical extinction from the DL model and that measured from the optical photometry of QSOs depends on U_{min}. We introduce the sample of QSOs we use in Sect. 6.1, and compare the DL and QSO A_V estimates in Sect. 6.2. Based on this analysis, we propose a renormalization of the optical extinction derived from the DL model (Sect. 6.3). The renormalized extinction map is compared to that derived by Schlafly et al. (2014, hereafterSGF) from stellar reddening using the Pan-STARRS1 (Kaiser et al. 2010) data.

6.1. The QSO sample

SDSS provides photometric observations for a sample of 272 366 QSOs, which allow us to measure the optical extinction for comparison with that from the DL model. A subsample of 105 783 (an earlier data release) was used in *Pl*-MBB to normalize the opacity maps derived from the MBB fits in order to produce an extinction map.

The use of QSOs as calibrators has several advantages over other cross-calibrations:

- QSOs are extragalactic, and at high redshift, so all the detected dust in a given pixel is between the QSO and us, a major advantage with respect to maps generated from stellar reddening studies;
- the QSO sample is large and well distributed across diffuse ($A_V \lesssim 1$) regions at high Galactic latitude, providing good statistics;
- SDSS photometry is very accurate and well understood.

In Appendix B we describe the SDSS QSO catalogue in detail, and how for each QSO we measure the extinction $A_{V,\mathrm{QSO}}$ from the optical SDSS observations.

6.2. $A_{V,\mathrm{QSO}} - A_{V,\mathrm{DL}}$ comparison

In this section, we present a comparison of the DL and QSO extinction, as a function of the fitted parameter U_{min}. The DL and

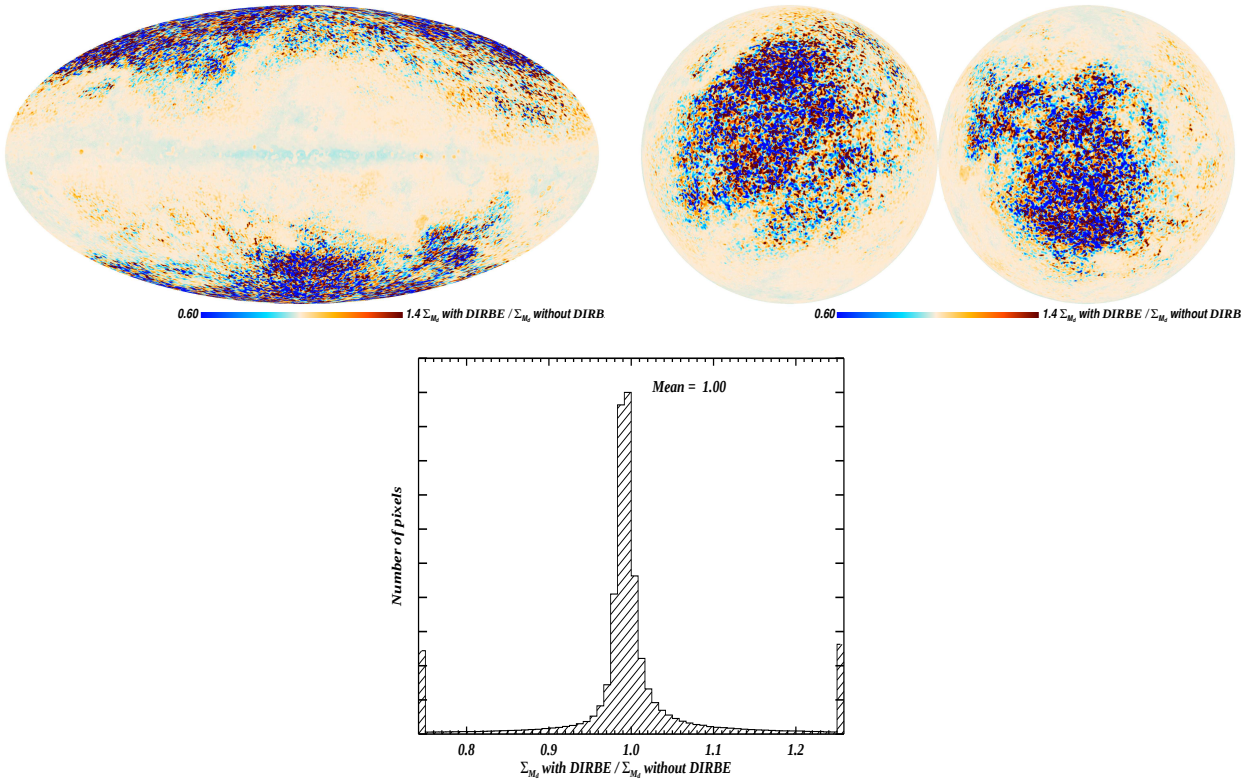

Fig. 7. Comparison between the dust mass estimates obtained with and without the DIRBE 140 and DIRBE 240 photometric constraints. The top row shows maps of the ratio between the two dust mass estimates, and the bottom row shows the corresponding histogram. Both model fits are performed using a 1° FWHM Gaussian PSF. The difference between the dust mass estimates is relatively small (within a few percent) and so it is safe to perform a modelling of the sky without the DIRBE constraints. In the bottom row, the points below 0.8 and over 1.2 were added to the 0.8 and 1.2 bars, respectively.

QSO estimates of A_V are compared in the following way. We sort the QSO lines of sight with respect of the $U_{\rm min}$ value and divide them in 20 groups having (approximately) equal number of QSOs each. For each group of QSOs, we measure the slope $\epsilon(U_{\rm min})$ fitting the $A_{V,\rm QSO}$ versus $A_{V,\rm DL}$ data with a line going through the origin. In Figure 9, $\epsilon(U_{\rm min})$ is plotted versus the mean value of $U_{\rm min}$ for each group. We observe that $\epsilon(U_{\rm min})$, a weighted mean of $A_{V,\rm QSO}/A_{V,\rm DL}$ in each $U_{\rm min}$ bin, depends on $U_{\rm min}$. The slope obtained fitting the $A_{V,\rm QSO}$ versus $A_{V,\rm DL}$ for the whole sample of QSOs is $\langle\epsilon\rangle \approx 0.495$. Therefore, on average the DL model overpredicts the observed $A_{V,\rm QSO}$ by a factor of $1/0.495 = 2.0$, with the discrepancy being larger for sightlines with smaller $U_{\rm min}$ values. There is a 20 % difference between the 2.4 factor that arises from the comparison between $A_{V,\rm DL}$ and $A_{V,\rm QSO}$ indirectly via the MBB A_V fit, and the mean factor of 2.0 found here. This is due to the use of a different QSO sample (*Pl*-MBB used a smaller QSO sample), which accounts for 10 % of the difference, and to differences in the way the QSO A_V is computed from the SDSS photometry, responsible of the remaining 10 %.

For a given FIR SED, the DL model predicts the optical reddening unambiguously, with no freedom for any extra calibration. However, if one had the option to adjust the DL extinction estimates by multiplying them by a single factor (i.e. ignoring the dependence of ϵ on $U_{\rm min}$), one would reduce the optical extinction estimates by a factor of 2.0.

6.3. Renormalization of the $A_{V,\rm DL}$ map in the diffuse ISM

We use the results of the $A_{V,\rm QSO} - A_{V,\rm DL}$ comparison (Section 6.2 and Figure 9) to renormalize the $A_{V,\rm DL}$ map in the diffuse ISM. The ratio between the two extinction values is well approximated as a linear function of $U_{\rm min}$:

$$A_{V,\rm QSO} \approx (0.42\,U_{\rm min} + 0.28)\,A_{V,\rm DL}, \quad (8)$$

Thus, we define a renormalized DL optical reddening as[14]:

$$A_{V,\rm RQ} = (0.42\,U_{\rm min} + 0.28) \times A_{V,\rm DL}. \quad (9)$$

Empirically, $A_{V,\rm RQ}$ is our best estimator of the QSO extinction $A_{V,\rm QSO}$. *Pl*-MBB proposed the dust radiance (the total luminosity emitted by the dust) as a tracer of dust column density in the diffuse ISM. This would be expected if the radiation field heating the dust were uniform, and the variations of the dust temperature were only driven by variation of the dust FIR-submm opacity in the diffuse ISM. The dust radiance is proportional to $U_{\rm min} \times A_{V,\rm DL}$. Our best fit of the renormalization factor as a function of $U_{\rm min}$ is an intermediate solution between the radiance and the model column density ($A_{V,\rm DL}$). The scaling factor in Eq. 8 increases with $U_{\rm min}$ but with a slope smaller than 1. Figure 9 shows that our renormalization is a better fit of the data than the radiance.

[14] We add the letter Q to indicate the renormalization using the $A_{V,\rm QSO}$.

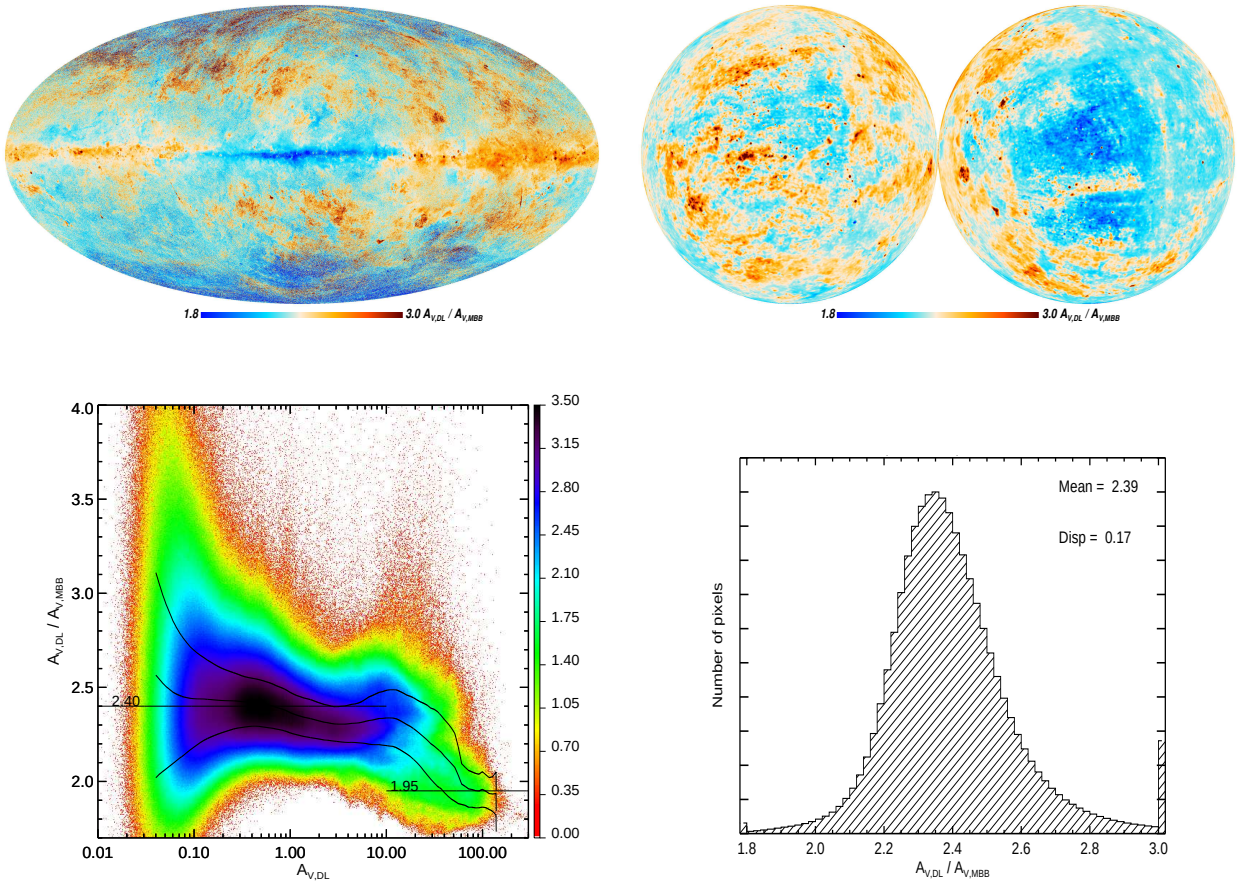

Fig. 8. Comparison between DL and MBB A_V estimates, denoted $A_{V,\mathrm{DL}}$ and $A_{V,\mathrm{MBB}}$ respectively. The top row shows the ratio of the $A_{V,\mathrm{MBB}}$ and $A_{V,\mathrm{DL}}$ maps. The polar projection maps are smoothed to 1° resolution to highlight the systematic departures. The bottom row shows the ratio of the $A_{V,\mathrm{MBB}}$ and $A_{V,\mathrm{DL}}$ estimates as a function of the $A_{V,\mathrm{DL}}$ estimate (left) and its histogram (right). In the bottom left panel the colour corresponds to the logarithm of the density of points (see Figure 5). The curves correspond to the mean value and the $\pm 1\,\sigma$ dispersion. The $A_{V,\mathrm{DL}}$ and $A_{V,\mathrm{MBB}}$ values used in this comparison are derived from a fit of the same data sets.

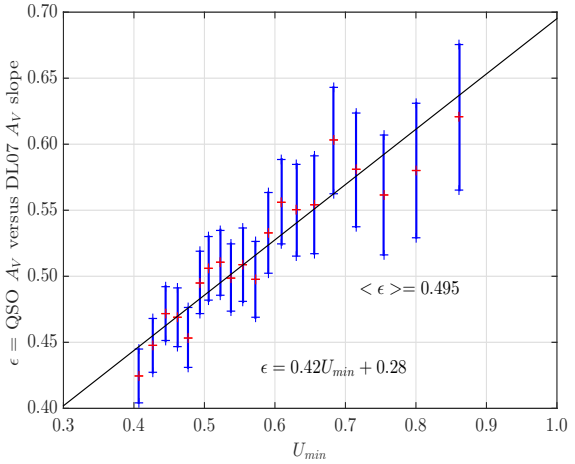

Fig. 9. Ratio between the QSO extinction estimates $A_{V,\mathrm{QSO}}$ and the DL extinction estimates $A_{V,\mathrm{DL}}$, as a function of the fitted parameter U_{min}. The ratio is the slope ϵ obtained fitting $A_{V,\mathrm{QSO}}$ versus $A_{V,\mathrm{DL}}$ in each U_{min} bin (see text). It is approximated by a linear function of U_{min}.

6.4. Validation of the renormalized extinction with stellar observations

We compare the renormalized extinction $A_{V,\mathrm{RQ}}$ to the extinction estimated by SGF from optical stellar observations, denoted $A_{V,\mathrm{Sch}}$. SGF presented a map of the dust reddening to 4.5 kpc derived from Pan-STARRS1 stellar photometry. Their map covers almost the entire sky north of declination −30° at a resolution of 7′ − 14′. In the present analysis, we discard the sky areas with $|b| < 5°$ to avoid the Galactic disk where a fraction of the dust is farther than 4.5 kpc, and therefore, traced by dust in emission, but not present in the SGF absorption map.

Figure 10 shows the comparison between the renormalized DL A_V estimates ($A_{V,\mathrm{RQ}}$) with the stellar observations based $A_{V,\mathrm{Sch}}$ estimates in the $|b| > 5°$ sky. The agreement between both $A_V$estimates is remarkable. The difference between the estimates ($A_{V,\mathrm{Sch}}$- $A_{V,\mathrm{RQ}}$) has a mean of 0.02 mag and scatter (variance) of 0.12 mag. This comparison validates our renormalized DL A_V estimates as a good tracer of the dust optical extinction in the $|b| > 5°$ sky. Our optical extinction estimate ($A_{V,\mathrm{RQ}}$) was tailored to match the QSOs A_V estimates. QSOs were observed in diffuse diffuse Galactic lines of sight (most of the QSOs have $A_V \approx 0.1$). The agreement of the $A_{V,\mathrm{Sch}}$ and $A_{V,\mathrm{RQ}}$ estimates extends the validity of the DL renormalized estimate ($A_{V,\mathrm{RQ}}$) to greater column densities. The scatter of $A_{V,\mathrm{Sch}}$- $A_{V,\mathrm{RQ}}$ provides an estimate of the uncertainties in the different A_V estimates.

7. FIR SEDs per unit of optical extinction

The DL model parameter U_{min} and the QSO data are used to compress the FIR IRAS and sub-mm Planck observations of the

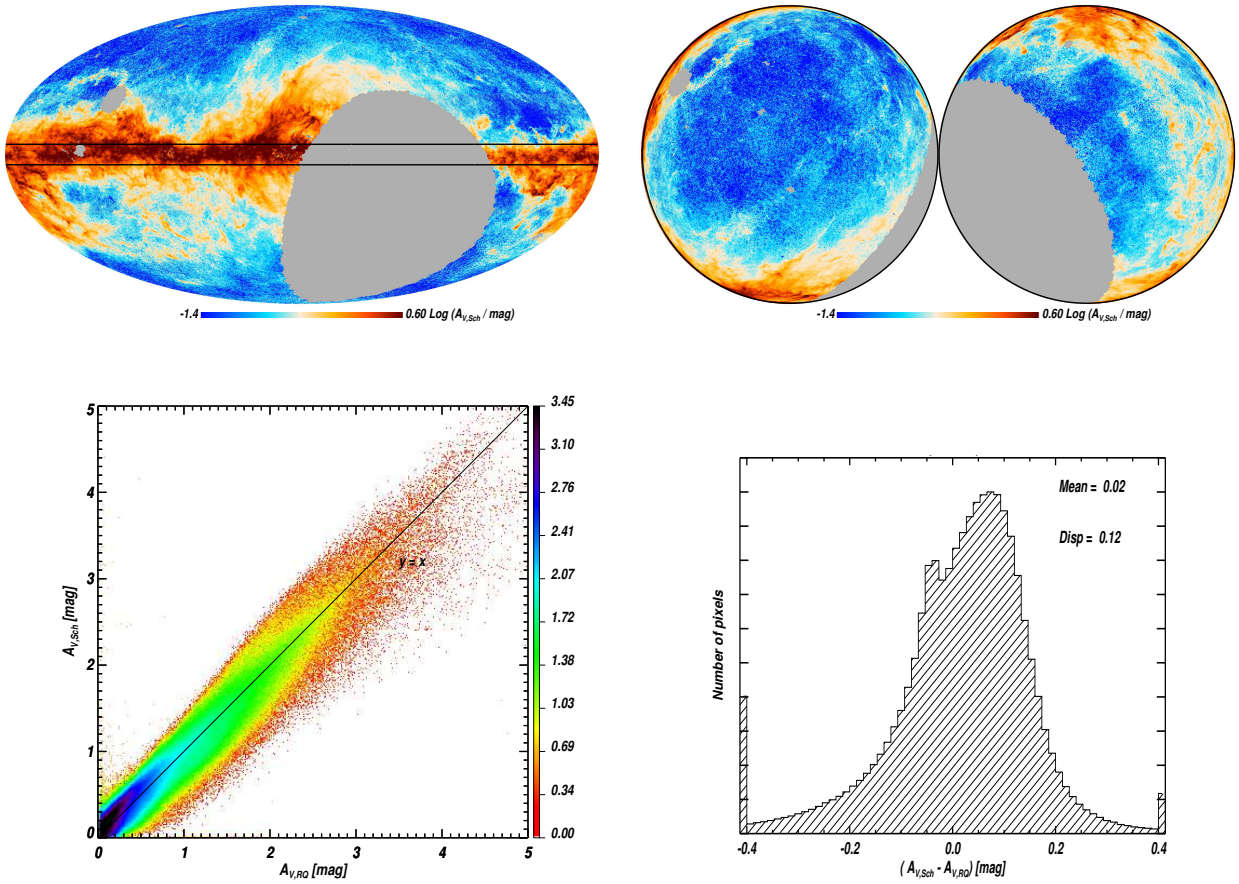

Fig. 10. Comparison between the renormalized DL A_V estimates ($A_{V,\mathrm{RQ}}$), and those derived from optical stellar observations ($A_{V,\mathrm{Sch}}$). The top row shows the A_V maps derived from optical stellar observations. The $b = \pm 5°$ lines have been added for reference. The bottom row left panel compares the renormalized $A_{V,\mathrm{RQ}}$ estimates with those derived from optical stellar observations $A_{V,\mathrm{Sch}}$ in the $|b| > 5°$ sky. The agreement of these independent A_V estimates is a successful test of our empirical renormalization. The bottom row right panel show the histogram of the difference of the two A_V estimates, also in the $|b| > 5°$ sky.

diffuse ISM to a set of 20 SEDs normalized per A_V, which we present and discuss.

The parameter U_{min} is mainly determined by the wavelength where the SED peaks; as a corollary, SEDs for different values of U_{min} differ significantly. The A_V values obtained from the QSO analysis, $A_{V,\mathrm{QSO}}$, allow us to normalize the observed SEDs (per unit of optical extinction) and generate a one-parameter family of I_ν/A_V. This family is indexed by the U_{min} parameter; the QSO lines of sight are grouped according to the fitted Galactic U_{min} value. We divide the sample of good QSOs in 20 bins, containing 11 212 QSOs each[15].

To obtain the I_ν/A_V values we proceed as follows. For each band and U_{min}, we would like to perform a linear regression of the I_ν values as a function of $A_{V,\mathrm{QSO}}$. The large scatter and non-Gaussian distribution of $A_{V,\mathrm{QSO}}$ and the scatter on I_ν make it challenging to determine such a slope robustly. Therefore, we smooth the maps to a Gaussian PSF with 30′ FWHM to reduce the scatter on I_ν, redo the dust modelling (to obtain a coherent U_{min} estimate), and perform the regression on the smoothed (less noisy) maps. The non-Gaussian distribution of $A_{V,\mathrm{QSO}}$ do not introduce any bias in the slope found[16].

Figure 11 presents the set of SEDs. The left panel shows the SEDs for the different U_{min} values. The right panel shows each SED divided by the mean to highlight the differences between the individual SEDs.

The complex statistics of the $A_{V,\mathrm{QSO}}$ estimates, which depend on variations in QSO intrinsic spectra, makes it hard to obtain a reliable estimate of the uncertainties in the (normalizing) A_V. However, the statistical uncertainties are not dominant because they average out thanks to the large size of the QSOs sample. The accuracy of our determination of the FIR intensities per unit of optical extinction is mainly limited by systematic uncertainties on the normalization by A_V. *Pl*-MBB estimated the A_V over a subsample of the QSOs, and their estimates differ from ours by $\approx 14\,\%$. When we compare our $A_{V,\mathrm{QSO}}$ estimates from those of SGF based on stellar photometry (Sect. 6.4), we find an agreement within 5−10% over the QSO lines of sight, Therefore, it is reasonable to assume our $A_{V,\mathrm{QSO}}$ estimates are uncertain at a 10% level. The instrumental calibration uncertainties ($\lesssim 6\%$ at *Planck* frequencies) translate directly to the FIR intensities per unit of optical extinction. Therefore, the normalization of each SED may be uncertain up to about $\approx 15\,\%$.

In Figure 12, the specific intensities per unit of optical extinction are compared with the DL model. The four panels correspond to the spectral bands: *IRAS* 100; *Planck* 857; *Planck* 545; and *Planck* 353. In each panel, the black curve corresponds to the DL intensity normalized by A_V, and the red curves to the DL intensity normalized by $A_{V,\mathrm{RQ}}$, i.e. the model intensity scaled by the renormalization factor in Eq. 8. The DL model

[15] A few of the bins contain 11 213 QSOs

[16] See discussion in Appendix B.2, and Figure B.2.

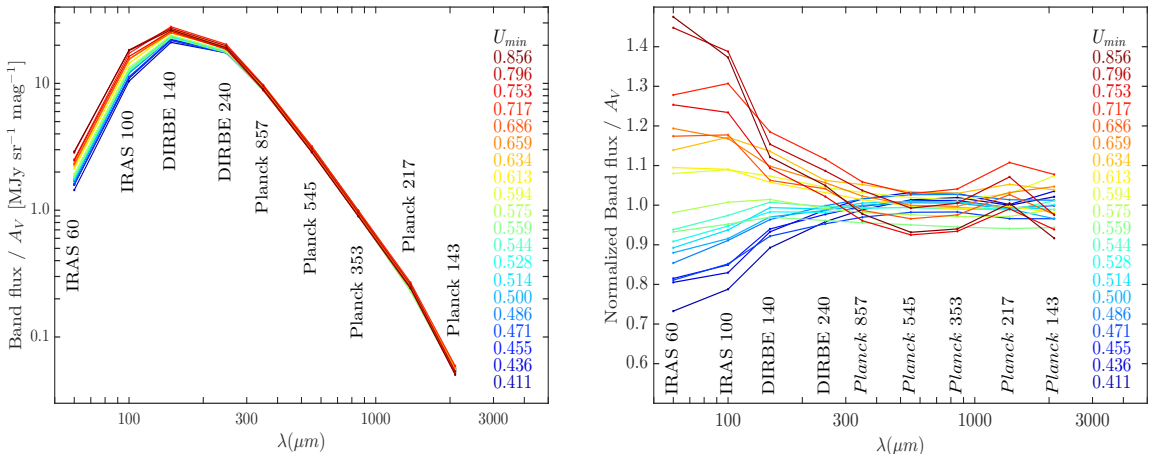

Fig. 11. FIR measured intensity per unit of optical extinction as a function of the fitted parameter $U_{\rm min}$. In the right panel, the SEDs are divided by the mean SED, i.e. normalized with the SED per unit of optical extinction obtained without binning on $U_{\rm min}$.

under-predicts the FIR intensities per unit of optical extinction A_V by significant amounts, especially for sightlines with low fitted values of $U_{\rm min}$, but the renormalization of the DL A_V values brings into agreement the observed and model band intensities per unit of extinction. This result shows that the DL model has approximately the correct SED shape to fit the measured SEDs for the diffuse ISM, and that a $U_{\rm min}$-dependent renormalization brings the DL model into agreement with the *IRAS* and *Planck* data. It is also a satisfactory check of the consistency of our data analysis and model fitting. Indeed, the SED values in Fig. 12 are derived from a linear fit between the data and $A_{V,\rm QSO}$, the renormalization factor from a linear fit between $A_{V,\rm QSO}$ and $A_{V,\rm DL}$ (see Fig. 9), and $A_{V,\rm DL}$ from the DL model fit of the data (see Sect. 3.2).

8. Optical extinction and FIR emission in molecular clouds

We extend our assessment of the DL extinction maps to molecular clouds using extinction maps from 2MASS stellar colours that are presented in Sect. 8.1. In Sect. 8.2, we compare them with the original and renormalized estimates derived from the DL model. We discuss a model renormalization for molecular clouds in Sect. 8.3.

8.1. Extinction maps of molecular clouds

Schneider et al. (2011) presented optical extinction maps, denoted $A_{V,\rm 2M}$, of several clouds computed using stellar observations from the 2MASS catalogue in the J, H, and K bands. We use the maps of the Cepheus, Chamaeleon, Ophiuchus, Orion, and Taurus cloud complexes. The Schneider et al. (2011) A_V maps were computed using a 2′ Gaussian PSF, and we smooth them to a 5′ Gaussian PSF to perform our analysis. We corrected the 2MASS maps for a zero level offset that is fitted with an inclined plane with an algorithm similar to the one used to estimate the background in the analysis of the KINGFISH sample of galaxies in AD12. The algorithm iteratively and simultaneously matches the zero level across the $A_{V,\rm RQ}$ and $A_{V,\rm 2M}$ maps and defines the areas that are considered background. The uncertainty on the zero level of the A_V maps is smaller than 0.1 magnitude. It is significant only for the map areas with the lowest A_V values.

Figure 13 shows the 2MASS $A_{V,\rm 2M}$ map, the DL $U_{\rm min}$ map, the $A_{V,\rm DL}$ map (divided by 3.07, see Section 8.2) and the renormalized $A_{V,\rm RQ}$ map for the Chamaeleon region. The inner (high A_V) areas correspond to the lowest $U_{\rm min}$ values, as expected since the stellar radiation field heating dust grains is attenuated when penetrating into molecular clouds. The cloud complexes show a similar $A_V - U_{\rm min}$ trend.

8.2. Comparison of 2MASS and DL extinction maps in molecular clouds

For each cloud, we find an approximate linear relation between the $A_{V,\rm 2M}$ and the $A_{V,\rm DL}$ maps as illustrated for the Chamaeleon cloud in the left panel of Fig. 14. After multiplicative adjustment, the $A_{V,\rm DL}$ and $A_{V,\rm 2M}$ estimates agree reasonably well. However, as in the diffuse ISM, the (FIR based) $A_{V,\rm DL}$ estimates are significantly larger than the (optical) $A_{V,\rm 2M}$ estimates. For the selected clouds, the DL model overestimates the 2MASS stellar A_V by factors of 2−3. Table 2 provides the multiplicative factors needed to make the 2MASS A_V maps agree with the DL A_V maps.

Table 2. Mean ratio between the DL and 2MASS extinction estimates in molecular clouds.

Cloud name	$A_{V,\rm DL}$ versus $A_{V,\rm 2M}$ slope[a]
Cepheus	2.87
Chamaeleon	3.07
Ophiuchus	2.23
Orion	2.83
Taurus	2.99

We compare the renormalized $A_{V,\rm RQ}$ versus $A_{V,\rm 2M}$ values in the right panel of Fig. 14 for the Chamaeleon cloud and in Fig. 15 for all of the clouds. We find that the model renormalization, computed to bring into agreement the DL and QSO A_V estimates in the diffuse ISM, also accounts quite well (within 10 %) for the discrepancies between 2MASS and DL A_V estimates in molecular clouds in the $0 < A_V < 3$ range, and even does passably well (within 30 %) up to $A_V \approx 8$.

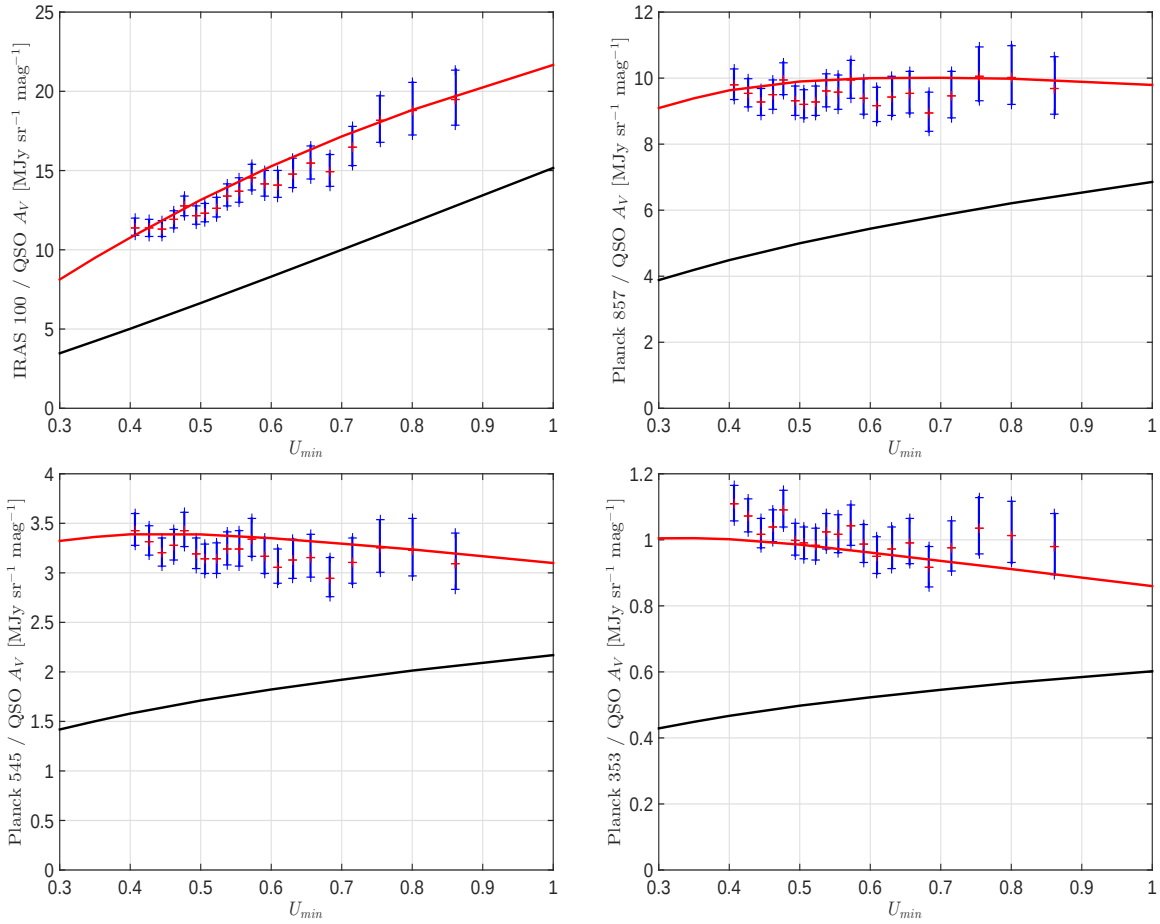

Fig. 12. The specific intensities per unit of optical extinction derived from a linear fit between the dust emission maps and $A_{V,\mathrm{QSO}}$ are plotted with red crosses and error bars in blue versus the fitted parameter U_{min}. The top row corresponds to *IRAS* 100 (left) and *Planck* 857 (right) and the bottom row to *Planck* 545 (left) and *Planck* 353 (right). The DL model values are plotted in black and the renormalized model in red. This plot shows that a U_{min}-dependent renormalization brings the DL model into agreement with the *IRAS* and *Planck* data.

8.3. Renormalization of $A_{V,\mathrm{DL}}$ in molecular clouds.

In the diffuse ISM analysis, we concluded that U_{min} is tracing variations in the radiation field and the dust opacity. Both phenomena are also present in molecular clouds, but their relative contribution in determining the SED peak (and therefore U_{min}) need not be the same as in the diffuse ISM. Therefore, a renormalization of the DL A_V based on 2MASS data may be different from that determined using the QSOs.

In Fig. 16 we compare the DL and 2MASS A_V estimates for pixels from the five cloud complexes with $1 < A_{V,2\mathrm{M}} < 5$. Similarly to Fig. 9, but using the 2MASS A_V estimates instead of those from QSOs, we plot the ratio $A_{V,\mathrm{DL}} / A_{V,2\mathrm{M}}$ as a function of the fitted U_{min}. For each U_{min} value, the solid curve corresponds to the best fit slope of the $A_{V,\mathrm{DL}}$ versus $A_{V,2\mathrm{M}}$ values (i.e. it is an estimate of a weighted mean of the $A_{V,\mathrm{DL}} / A_{V,2\mathrm{M}}$ ratio). The straight solid line corresponds to a fit to the solid curve in the $0.2 < U_{\mathrm{min}} < 1.0$ range. In this fit, each U_{min} is given a weight proportional to the number of pixels that have this value in the clouds (i.e. most of the weight is for the pixels within the $0.2 < U_{\mathrm{min}} < 0.8$ range). The dashed line corresponds to the renormalization proposed in Section 6.3 (Eq. 9) for the diffuse ISM.

The straight line in Fig. 16 corresponds to a renormalization tailored to bring into agreement the $A_{V,\mathrm{DL}}$ and $A_{V,2\mathrm{M}}$ estimates, i.e. a 2MASS renormalization for molecular clouds, denoted $A_{V,\mathrm{RC}}$. The 2MASS renormalization is given by

$$A_{V,\mathrm{RC}} = (0.38\,U_{\mathrm{min}} + 0.27) \times A_{V,\mathrm{DL}}. \quad (10)$$

Empirically, $A_{V,\mathrm{RC}}$ is our best estimator of the 2MASS extinction $A_{V,2\mathrm{M}}$. It is satisfactory for the renormalization method to find that the 2MASS normalization factor for molecular clouds is quite close to the one for the diffuse ISM.

9. Discussion

In Sects. 9.1 and 9.2, we relate the difference between the DL model and A_V estimates from QSO observations to dust emission properties and their evolution within the diffuse ISM. The renormalization method we propose to correct empirically for this discrepancy is discussed in Section 9.3.

9.1. DL FIR emission and optical extinction disagreement

In the diffuse ISM, the DL model provides good fits to the SED of Galactic dust from *WISE*, *IRAS*, and *Planck*data, as it has been the case in the past for external galaxies observed with *Spitzer* and *Herschel*. However, the fit is not fully satisfactory because the A_V values from the model do not agree with those derived from optical colours of QSOs for the diffuse ISM and stars for molecular clouds. The optical extinction discrepancy can be decomposed in two levels: (1) the mean factor of 1.9 between the

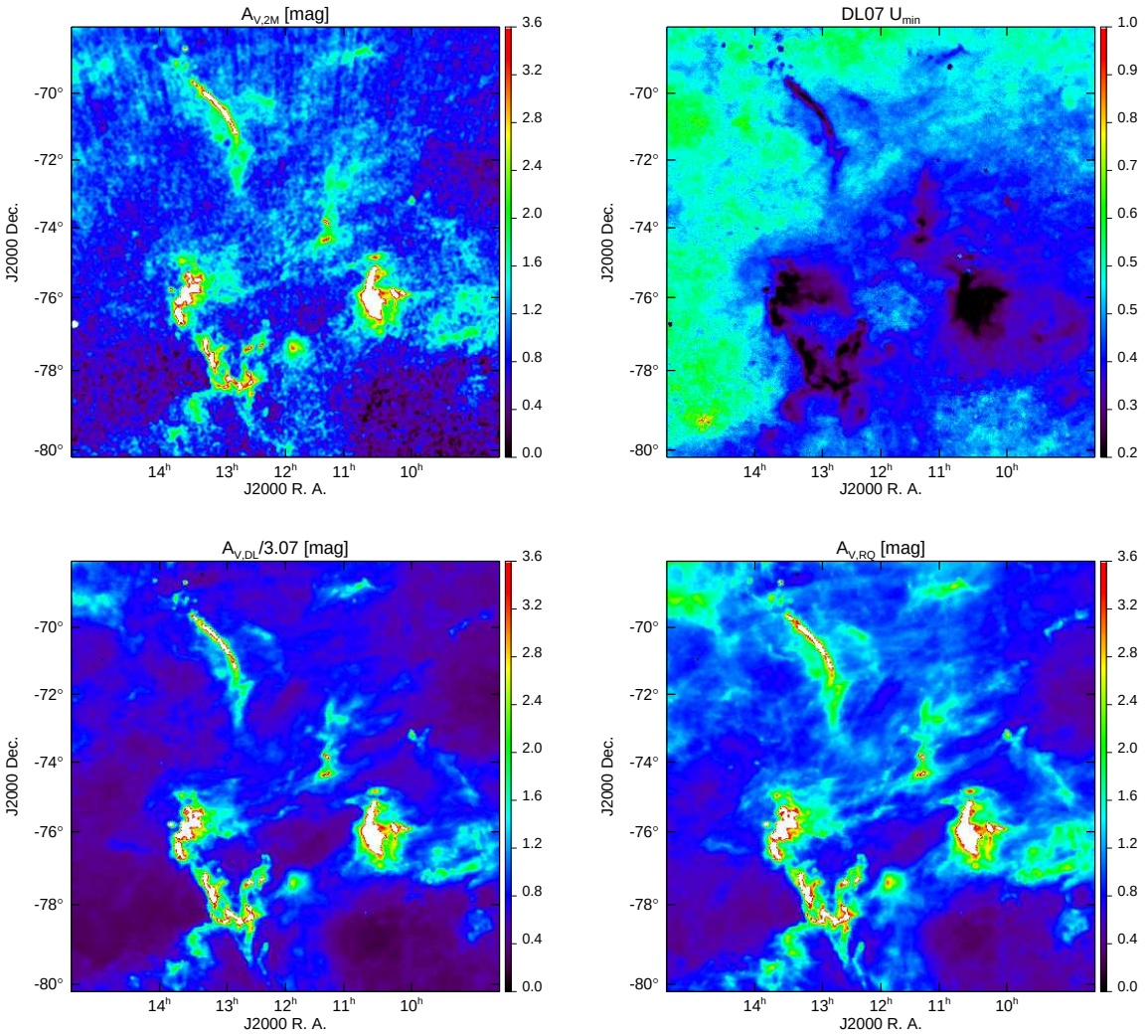

Fig. 13. 2MASS and DL estimates in the Chamaeleon cloud region. The top row shows the (background corrected) 2MASS $A_{V,2M}$ map (left) and the DL $U_{\rm min}$ map (right). The bottom row shows the DL $A_{V,\rm DL}$ estimate divided by 3.07 (left), and the renormalized model $A_{V,\rm RQ}$ estimates (right). (See Section 8.2 for a derivation of the 3.07 factor)

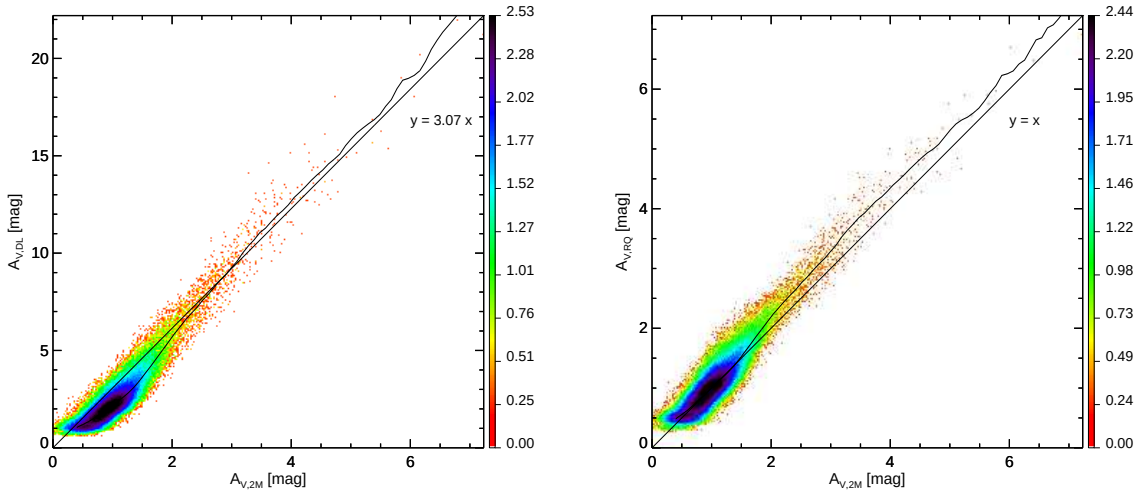

Fig. 14. 2MASS and DL A_V comparison in the Chamaeleon cloud. The left panel shows the $A_{V,\rm DL}$ versus $A_{V,2M}$ values, and the right panel the renormalized $A_{V,\rm RQ}$ versus $A_{V,2M}$ values. The diagonal lines correspond to $y = 3.07x$, and $y = x$ respectively, and the curves correspond to the mean value.

Table 3. FIR SEDs per unit of optical extinction[a]

SED #	DL fit $U_{\rm min}$	DL fit $\Sigma^{\rm b}_{L_{\rm d}}$ [$10^7 L_\odot$ kpc^{-2}mag^{-1}]	Intensity per A_V [MJy sr^{-1} mag^{-1}] *Planck* 143[c]	*Planck* 217[c]	*Planck* 353	*Planck* 545	*Planck* 857	*IRAS* 100	*IRAS* 60
1	0.4178	2.28	0.0506	0.221	0.937	3.22	9.33	10.2	2.20
2	0.4674	2.33	0.0509	0.211	0.908	3.17	9.36	10.8	2.27
3	0.4984	2.39	0.0488	0.208	0.901	3.15	9.36	11.4	2.39
4	0.5207	2.54	0.0510	0.215	0.933	3.27	9.73	12.4	2.67
5	0.5407	2.46	0.0490	0.205	0.894	3.14	9.35	12.2	2.46
6	0.5602	2.62	0.0505	0.215	0.935	3.28	9.77	13.2	2.93
7	0.5793	2.73	0.0512	0.219	0.954	3.36	10.1	14.0	2.82
8	0.5984	2.65	0.0529	0.211	0.912	3.22	9.64	13.7	2.99
9	0.6182	2.67	0.0498	0.207	0.899	3.18	9.54	14.0	2.76
10	0.6383	2.80	0.0496	0.211	0.928	3.28	9.90	14.9	2.92
11	0.6590	2.98	0.0549	0.220	0.963	3.41	10.3	15.9	3.16
12	0.6810	2.89	0.0486	0.207	0.914	3.25	9.86	15.7	3.11
13	0.7056	3.01	0.0507	0.210	0.926	3.29	10.0	16.4	3.29
14	0.7333	3.14	0.0494	0.213	0.945	3.36	10.3	17.3	3.51
15	0.7644	3.35	0.0509	0.214	0.944	3.36	10.3	18.2	4.40
16	0.7960	3.23	0.0492	0.208	0.921	3.29	10.1	18.3	3.75
17	0.8289	3.21	0.0467	0.202	0.898	3.21	9.93	18.5	3.77
18	0.8673	3.13	0.0465	0.191	0.848	3.04	9.50	18.2	3.77
19	0.9123	3.31	0.0445	0.194	0.868	3.13	9.82	19.5	4.11
20	0.9776	3.27	0.0415	0.180	0.802	2.91	9.19	19.2	4.32
Dispersion within each bin[d] [%]			41.	13.	4.7	3.1	4.4	7.7	29.

a The SEDs in this Table were obtained fitting the same *Planck* and *IRAS* data as in *Pl*-MBB (see Sect. 2).
b Bolometric dust emission per unit A_V computed from the DL fit.
c The specific intensities for the *Planck* 217 and 143 bands were not used to constrain the DL model.
d Dispersion of the specific intensities normalized by $\Sigma_{L_{\rm d}}$ computed over sky pixels within a given $U_{\rm min}$ bin. We list the mean standard deviation for each frequency since the measured dispersions are similar for the different $U_{\rm min}$ bins. The scatter is the largest at 143 and 217 GHz due to the statistical noise in the *Planck* data, and at 60 μm due to variations in $f_{\rm PDR}$.

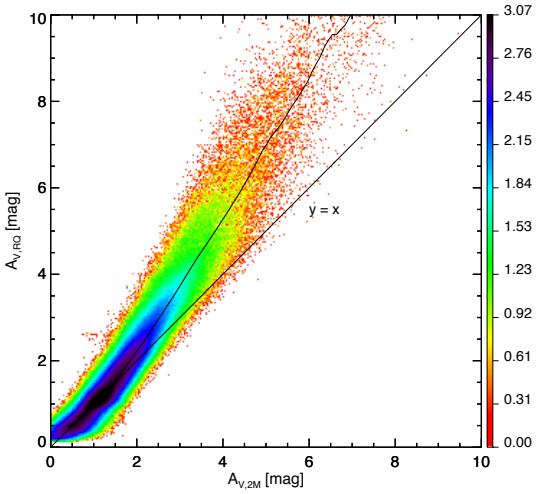

Fig. 15. Comparison of the renormalized $A_{V,\rm RQ}$ and 2MASS $A_{V,2\rm M}$ estimates. The individual pixels of the Cepheus, Chamaeleon, Ophiuchus, Orion, and Taurus clouds are combined. Colour corresponds to the logarithm of the density of points (see Figure 5). The diagonal line corresponds to $y = x$, and the curve to the mean value.

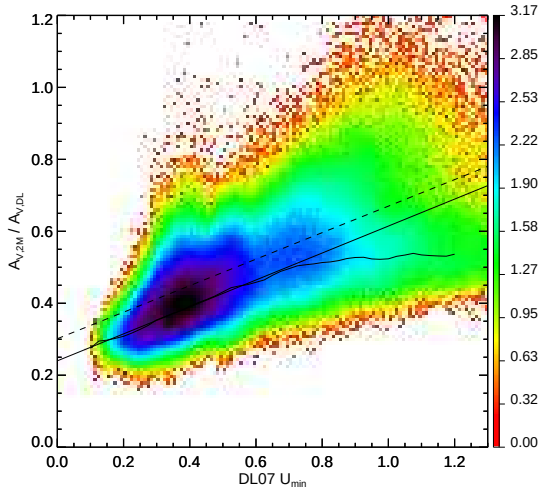

Fig. 16. Renormalization of the DL A_V values in molecular clouds. Pixels from the five molecular complexes with $1 < A_{V,2\rm M} < 5$ are included here. Colours encode the logarithm of the density of points (see Figure 5). For each $U_{\rm min}$ value, the solid curve corresponds to the best fit slope of the $A_{V,\rm DL}$ versus $A_{V,2\rm M}$ values. The straight solid line corresponds to a fit to the solid curve in the $0.2 < U_{\rm min} < 1.0$ range, where each $U_{\rm min}$ is given a weight proportional to the number of pixels that have this value in the clouds. The straight solid line provides the $A_{V,\rm RC}$ renormalization, and the dashed line that derived from the QSO analysis.

DL and QSOs A_V values, and (2) the dependence of the ratio between the DL and QSO A_V values on $U_{\rm min}$.

The result of the SED fit depends on the spectral shape of the dust opacity. A spectral difference makes the DL model fit with a lower $U_{\rm min}$ value than the true radiation field intensity, which turns into an increase of the A_V estimates[17]. The mean factor

[17] For example, if an MBB with T = 19K, $\beta = 1.9$ is fitted with an MBB with $\beta = 1.8$, using the *IRAS* 100, *Planck* 857, *Planck* 545, and

between the DL and QSOs A_V values could also be indicating that the DL dust material has a FIR–submm opacity per unit of optical extinction that is too low.

The dependency of the ratio between the DL and QSO A_V values on $U_{\rm min}$ shows that variations in the value of the FIR–submm dust opacity per unit of optical extinction, or its spectral shape, are needed across the sky; we take this to be evidence of dust evolution. This discrepancy will be present for all dust models based on fixed dust optical properties, possibly with a different magnitude depending of the details of the specific model.

Fanciullo et al. (2015) have used three dust models, the DL, Compiègne et al. (2011) and Jones et al. (2013) models, to fit the Planck SEDs in Table 3 and compare results. We note that the SEDs listed in the Table and used by Fanciullo et al. (2015) are the DL model results obtained fitting the same *Planck* and *IRAS* data as in *Pl*-MBB (see Sect. 2). This study, a follow-up of our data analysis, confirms our interpretation of our DL modelling in two ways. First, the mean ratio between the model and QSO A_V values is different for each model. The best match between model and data is obtained for the model of Jones et al. (2013), which uses a FIR–submm opacity per unit of optical extinction[18] larger than that of the DL model. Second, the three models fail in the same way to reproduce the variations in the emission per unit extinction with a variable ISRF intensity.

Fanciullo et al. (2015) also present fits of the Planck SEDs in Table 3 with a MBB spectrum (see their Appendix A). The dust FIR–submm opacity per unit extinction and the temperature obtained from these empirical fits display the same anti-correlation as that observed for the dust models between A_V and the ISRF intensity. Thus, the dust models and MBB fits provide the same evidence for changes in the FIR–submm dust opacity in the diffuse ISM. Fanciullo et al. (2015) estimate that the amplitude of the variations must be $\sim$ 20% to account for the typical ($\pm1\sigma$ around the mean) variations of the dust SEDs, and 40-50% for the full range.

9.2. Dust evolution in the diffuse ISM

We relate the Planck evidence for variations of the FIR–submm dust opacity to earlier studies of dust evolution in the ISM.

The extinction curve is known to vary through the ISM (Cardelli et al. 1989; Fitzpatrick & Massa 2007), especially in the UV but also in the near-IR (Fitzpatrick & Massa 2009). Similarly, the mid-IR dust emission presents variations of colour ratios between bands (Miville-Deschênes et al. 2002; Flagey et al. 2009). It is one of the successes of models like DL07 to be able accommodate this kind of evolution by adapting the size distribution of each component (Weingartner & Draine 2001), as well as the radiation field intensity for emission.

With the observations of far-infrared dust emission by the ISOPHOT camera onboard ISO and the PRONAOS balloon, it was however demonstrated that adapting the size distribution could not explain the low grain temperatures observed in dense filaments (Del Burgo et al. 2003; Stepnik et al. 2003). These papers argue that the intrinsic dust opacity in the far-infrared increases by a factor of a few, and that this can be achieved by modifying the grain structure and composition itself. Indeed, dust is known to be more emissive as composite aggregates than as compact grains (Stognienko et al. 1995; Köhler et al. 2011). The number of observations has since increased and confirmed this tendency (Del Burgo & Laureijs 2005; Ridderstad et al. 2006; Collaboration et al. 2011), but primarily in the dense ISM (A_V larger than a few magnitudes). More recently with Spitzer and *Planck* observations such variations in the dust far-infrared opacity have been identified in the diffuse ISM, with amplitudes comparable to those observed before in the dense medium (Bot et al. 2009; Martin et al. 2012; Planck Collaboration XI 2014; Planck Collaboration Int. XVII 2014).

It is reasonable to accommodate the increase of dust opacity in the dense ISM by invoking coagulation (Köhler et al. 2011; Ysard et al. 2012; Ysard et al. 2013). However, dust models face now a new challenge. Since the timescale for dust coagulation increases for decreasing density, this solution does not hold in the diffuse, low-density, ISM. Variations in grain mantles composition and thickness through the accretion of carbon and cumulative irradiation have been proposed by Jones et al. (2013) and Ysard et al. (2015) as a main dust evolutionary process within the diffuse ISM. Differences in the past history of dust grains, i.e. in their evolutionary cycle between the diffuse ISM and molecular clouds, could also contribute to the observed scatter in the shape, size and composition of dust grains in the diffuse ISM (Martin et al. 2012). Modelling is needed to test whether these ideas can match the signature of dust evolution reported in this paper.

9.3. Optical exctinction A_V estimates of dust models

To obtain an accurate A_V map of the sky, we proposed two renormalizations of the A_V estimates derived from the DL model ($A_{V,\rm RQ}$ in Eq. 9 and $A_{V,\rm RC}$ in 10) that compensates for the discrepancy between the observed FIR emission and the optical extinction for the diffuse ISM and molecular clouds. Essentially, the renormalization rescales one of the model outputs (the dust optical extinction A_V) by a function of $U_{\rm min}$, to match data. Planck Collaboration Int. XXVIII (2015) presented an independent comparison of the renormalized $A_{V,\rm RQ}$ estimates with $\gamma-$ray observations in the Chamaeleon cloud. They concluded that the renormalized $A_{V,\rm RQ}$ estimates are in closer agreement with $\gamma-$ray A_V estimates than the (non-renormalized) $A_{V,\rm DL}$ estimates. We now discuss the model renormalization in a more general context.

The renormalized DL estimates ($A_{V,\rm RQ}$ and $A_{V,\rm RC}$) provide a good A_V determination in the areas where they were calibrated, but they do not provide any insight into the physical dust properties per se; the renormalized dust model becomes simply a family of SEDs used to fit the data, from which we construct and calibrate an observable quantity ($A_{V,\rm RQ}$ and $A_{V,\rm RC}$). Unfortunately, the fitted parameters of the renormalized model ($U_{\rm min}$) lack a physical interpretation: $U_{\rm min}$ is not solely tracing the heating intensity of the radiation field, as assumed in DL.

The A_V estimate of the DL dust model is a function of its fitted parameters, i.e. $A_V = f(\Sigma_{M_{\rm d}}, q_{\rm PAH}, \gamma, U_{\rm min})$. In general, if we fit a dust model with several parameters, A_V will be a function of the most relevant parameters[19]. The DL model assumes $A_V = f(\Sigma_{M_{\rm d}}) = k \times \Sigma_{M_{\rm d}}$, with $k = 0.74 \times 10^{-5}$ mag $\mathrm{M}_\odot^{-1}$ kpc^2. Our proposed renormalizations are a first step towards a functional renormalization by extending $A_V = k \times \Sigma_{M_{\rm d}}$ into $A_V = g(U_{\rm min}) \times k \times \Sigma_{M_{\rm d}}$, where we take $g(U_{\rm min})$ to be a linear function of $U_{\rm min}$. Due to the larger scatter in the QSO A_V estimates, only

Planck 353 bands, then the fitted amplitude will be 30 % larger than the original one. Therefore, a discrepancy of $\delta\Upsilon = 0.1$ is likely to produce a bias in the A_V estimates of the order of 30 %.

[18] The dust optical properties from this model are derived from recent laboratory data on silicates and amorphous carbons.

[19] In the MBB approach, one should consider a function of the form $A_V = f(\tau_{353}, T, \beta)$.

a simple linear function $g(U_{\rm min})$ can be robustly estimated in the diffuse ISM. In molecular clouds, where the data are less noisy, one could find a smooth function $g'(U_{\rm min})$, which better matches the $A_{V,\rm DL}$ / $A_{V,\rm 2M}$ fit for each $U_{\rm min}$ (i.e. in Figure 16, the solid curve flattens for $U_{\rm min} > 0.8$, departing from its linear fit).

Unfortunately any renormalization procedure, while leading to a more accurate A_V estimate, does not provide any further insight into the dust physical properties. Real physical knowledge will arise from a new generation of dust models that should be able to predict the correct optical extinction A_V from first principles. The next generation of dust models should be able to fit the empirical SEDs presented in Sect. 7 directly. While such a new generation of dust models is not yet available, we can for now correct for the systematic departures via Eqs. 9 and 10 for the diffuse ISM and molecular clouds, respectively.

10. Conclusions

We present a full-sky dust modelling of the new *Planck* data, combined with ancillary *IRAS* and *WISE* data, using the DL dust model. We test the model by comparing these maps with independent estimates of the dust optical extinction A_V using SDSS QSO photometry and 2MASS stellar data. Our analysis provides new insight on interstellar dust and a new A_V map over the full sky.

The DL model fits the observed *Planck*, *IRAS*, and *WISE* SEDs well over most of the sky. The modelling is robust against changes in the angular resolution, as well as adding DIRBE 140 and DIRBE 240 photometric constraints. The high resolution parameter maps that we generated trace the Galactic dusty structures well, using a state-of-the-art dust model.

In the diffuse ISM, the DL A_V estimates are larger than estimates from QSO optical photometry by approximately a factor of 2, and this discrepancy depends systematically on $U_{\rm min}$. In molecular clouds, the DL A_V estimates are larger than estimates based on 2MASS stellar colours by a factor of about 3. Again, the discrepancy depends in a similar way on $U_{\rm min}$.

We conclude that the current parameter $U_{\rm min}$, associated with the peak wavelength of the SED, does not trace only variations in the intensity of the radiation field heating the dust; $U_{\rm min}$ also traces dust evolution: i.e. variations in the optical and FIR properties of the dust grains in the diffuse ISM. DL is a physical dust model. Physical dust models have the advantage that, if successful, they give some support to the physical assumptions made about the interstellar dust and ISM properties that they are based on. Unfortunately, the deficiency found in this study indicates that some of the physical assumptions of the model need to be revised.

We provide a one-parameter family of SEDs per unit of dust optical extinction in the diffuse ISM. These SEDs, which relate the dust emission and absorption properties, are independent of the dust/gas ratio or problems inferring total H column density from observations. The next generation of dust models will need to reproduce these new SED estimates.

We propose an empirical renormalization of the DL A_V map as a function of the DL $U_{\rm min}$ parameter. The proposed renormalization ($A_{V,\rm RQ}$), derived to match the QSO A_V estimates for the diffuse ISM, also brings into agreement the DL A_V estimates with those derived from stellar colours for the $|b| > 5$ deg sky using the Pan-STARRS1 data (SGF), and towards nearby molecular clouds in the $0 < A_V < 5$ range using the 2MASS survey. We propose a second renormalized DL A_V estimate ($A_{V,\rm RC}$) tailored to trace the A_V estimates in molecular clouds more precisely.

The renormalized map $A_{V,\rm RQ}$ based on our QSOs analysis is our most accurate estimate of the optical extinction in the diffuse ISM. Comparison of the $A_{V,\rm RQ}$ map against other tracers of interstellar extinction that probe different environments, would further test its accuracy and check for any potential systematics. A comparison with *Fermi* data towards the Chamaeleon molecular cloud shows that the $A_{V,\rm RQ}$ map more closely matches the γ − ray diffuse emission than the 353 GHz opacity and radiance maps from *Pl*-MBB, but not as well as the fit obtained combining H I, CO, and dark neutral medium maps, which indicates significant differences in the FIR-submm dust emission properties between these gas components not taken into account in our renormalization (Planck Collaboration Int. XXVIII 2015).

Acknowledgements. The development of *Planck* has been supported by: ESA; CNES and CNRS/INSU-IN2P3-INP (France); ASI, CNR, and INAF (Italy); NASA and DoE (USA); STFC and UKSA (UK); CSIC, MICINN, JA, and RES (Spain); Tekes, AoF, and CSC (Finland); DLR and MPG (Germany); CSA (Canada); DTU Space (Denmark); SER/SSO (Switzerland); RCN (Norway); SFI (Ireland); FCT/MCTES (Portugal); and PRACE (EU). A description of the Planck Collaboration and a list of its members, including the technical or scientific activities in which they have been involved, can be found at `http://www.sciops.esa.int/index.php?project=planck&page=Planck_Collaboration`. The research leading to these results has received funding from the European Research Council under the European Union's Seventh Framework Programme (FP7/2007-2013) / ERC grant agreement n 267934.

References

Abazajian, K. N., Adelman-McCarthy, J. K., Agüeros, M. A., et al. 2009, ApJS, 182, 543
Aniano, G., Draine, B. T., Calzetti, D., et al. 2012, ApJ, 756, 46
Aniano, G., Draine, B. T., Calzetti, D., et al. 2015, in preparation
Boggess, N. W., Mather, J. C., Weiss, R., et al. 1992, ApJ, 397, 420
Bohlin, R. C., Savage, B. D., & Drake, J. F. 1978, ApJ, 224, 132
Boselli, A., Eales, S., Cortese, L., et al. 2010, PASP, 122, 261
Bot, C., Helou, G., Boulanger, F., et al. 2009, ApJ, 695, 469
Cardelli, J. A., Clayton, G. C., & Mathis, J. S. 1989, The Astrophysical Journal, 345, 245
Ciesla, L., Boquien, M., Boselli, A., et al. 2014, A&A, 565, A128
Collaboration, P., Abergel, A., Ade, P. A. R., et al. 2011, Astronomy and Astrophysics, 536, 25
Compiègne, M., Verstraete, L., Jones, A., et al. 2011, A&A, 525, A103
de Vaucouleurs, G., de Vaucouleurs, A., Corwin, Jr., H. G., et al. 1991, Third Reference Catalogue of Bright Galaxies (New York: Springer)
Del Burgo, C. & Laureijs, R. J. 2005, Monthly Notices of the Royal Astronomical Society, 360, 901
Del Burgo, C., Laureijs, R. J., Ábrahám, P., & Kiss, C. 2003, Monthly Notices of the Royal Astronomical Society, 346, 403
Desert, F.-X., Boulanger, F., & Puget, J. L. 1990, A&A, 237, 215
Doi, Y., Takita, S., Ootsubo, T., et al. 2015, PASJ, 67, 50
Draine, B. T., Aniano, G., Krause, O., et al. 2014, ApJ, 780, 172
Draine, B. T., Dale, D. A., Bendo, G., et al. 2007, ApJ, 663, 866
Draine, B. T. & Hensley, B. 2012, ApJ, 757, 103
Draine, B. T. & Lee, H. M. 1984, ApJ, 285, 89
Draine, B. T. & Li, A. 2007, ApJ, 657, 810
Dwek, E. 1998, ApJ, 501, 643
Fanciullo, L., Guillet, V., Aniano, G., et al. 2015, A&A, in press
Fazio, G. G., Hora, J. L., Allen, L. E., et al. 2004, ApJS, 154, 10
Finkbeiner, D. P., Davis, M., & Schlegel, D. J. 1999, ApJ, 524, 867
Fitzpatrick, E. L. 1999, PASP, 111, 63
Fitzpatrick, E. L. & Massa, D. 2007, The Astrophysical Journal, 663, 320
Fitzpatrick, E. L. & Massa, D. 2009, ApJ, 699, 1209
Flagey, N., Noriega-Crespo, A., Boulanger, F., et al. 2009, The Astrophysical Journal, 701, 1450
Górski, K. M., Hivon, E., Banday, A. J., et al. 2005, ApJ, 622, 759
Griffin, M. J., Abergel, A., Abreu, A., et al. 2010, A&A, 518, L3
Jones, A. P., Fanciullo, L., Köhler, M., et al. 2013, Astronomy and Astrophysics, 558, 62
Kaiser, N., Burgett, W., Chambers, K., et al. 2010, in Society of Photo-Optical Instrumentation Engineers (SPIE) Conference Series, Vol. 7733, Society of Photo-Optical Instrumentation Engineers (SPIE) Conference Series, 0
Kawada, M., Baba, H., Barthel, P. D., et al. 2007, PASJ, 59, 389

Kennicutt, R. C., Armus, L., Bendo, G., et al. 2003, PASP, 115, 928
Kennicutt, R. C., Calzetti, D., Aniano, G., et al. 2011, PASP, 123, 1347
Köhler, M., Guillet, V., & Jones, A. 2011, Astronomy and Astrophysics, 528, 96
Li, A. & Draine, B. T. 2001, ApJ, 554, 778
Liszt, H. 2014a, ApJ, 783, 17
Liszt, H. 2014b, ApJ, 780, 10
Martin, P. G., Roy, A., Bontemps, S., et al. 2012, ApJ, 751, 28
Mathis, J. S., Mezger, P. G., & Panagia, N. 1983, A&A, 128, 212
Meisner, A. M. & Finkbeiner, D. P. 2014, ApJ, 781, 5
Miville-Deschênes, M.-A., Boulanger, F., Joncas, G., & Falgarone, E. 2002, Astronomy and Astrophysics, 381, 209
Miville-Deschênes, M.-A. & Lagache, G. 2005, ApJS, 157, 302
Murakami, H., Baba, H., Barthel, P., et al. 2007, PASJ, 59, 369
Neugebauer, G., Habing, H. J., van Duinen, R., et al. 1984, ApJ, 278, L1
Pâris, I., Petitjean, P., Aubourg, É., et al. 2014, A&A, 563, A54
Pilbratt, G. L., Riedinger, J. R., Passvogel, T., et al. 2010, A&A, 518, L1
Planck Collaboration XVII. 2011, A&A, 536, A17
Planck Collaboration XXIV. 2011, A&A, 536, A24
Planck Collaboration I. 2014, A&A, 571, A1
Planck Collaboration VIII. 2014, A&A, 571, A8
Planck Collaboration XI. 2014, A&A, 571, A11
Planck Collaboration XIV. 2014, A&A, 571, A14
Planck Collaboration I. 2016, A&A, submitted
Planck Collaboration VIII. 2016, A&A, in press
Planck Collaboration IX. 2016, A&A, submitted
Planck Collaboration Int. XVII. 2014, A&A, 566, A55
Planck Collaboration Int. XXV. 2015, A&A, 582, A28
Planck Collaboration Int. XXVIII. 2015, A&A, 582, A31
Poglitsch, A., Waelkens, C., Geis, N., et al. 2010, A&A, 518, L2
Ridderstad, M., Juvela, M., Lehtinen, K., Lemke, D., & Liljeström, T. 2006, Astronomy and Astrophysics, 451, 961
Rieke, G. H., Young, E. T., Engelbracht, C. W., et al. 2004, ApJS, 154, 25
Schlafly, E. F., Green, G., Finkbeiner, D. P., et al. 2014, ApJ, 789, 15
Schlegel, D. J., Finkbeiner, D. P., & Davis, M. 1998, ApJ, 500, 525
Schneider, N., Bontemps, S., Simon, R., et al. 2011, A&A, 529, A1
Siebenmorgen, R., Voshchinnikov, N. V., & Bagnulo, S. 2014, A&A, 561, A82
Silverberg, R. F., Hauser, M. G., Boggess, N. W., et al. 1993, SPIE, 2019, 180
Skrutskie, M. F., Cutri, R. M., Stiening, R., et al. 2006, AJ, 131, 1163
Stepnik, B., Abergel, A., Bernard, J.-P., et al. 2003, Astronomy and Astrophysics, 398, 551
Stognienko, R., Henning, T., & Ossenkopf, V. 1995, Astronomy and Astrophysics, 296, 797
Vanden Berk, D. E., Richards, G. T., Bauer, A., et al. 2001, AJ, 122, 549
Vilardell, F., Ribas, I., Jordi, C., Fitzpatrick, E. L., & Guinan, E. F. 2010, A&A, 509, A70
Weingartner, J. C. & Draine, B. T. 2001, ApJ, 548, 296
Werner, M. W., Roellig, T. L., Low, F. J., et al. 2004, ApJS, 154, 1
Wright, E. L., Eisenhardt, P. R. M., Mainzer, A. K., et al. 2010, AJ, 140, 1868
York, D. G., Adelman, J., John E. Anderson, J., et al. 2000, The Astronomical Journal, 120, 1579
Ysard, N., Abergel, A., Ristorcelli, I., et al. 2013, A&A, 559, 133
Ysard, N., Juvela, M., Demyk, K., et al. 2012, A&A, 542, A21
Ysard, N., Köhler, M., Jones, A., et al. 2015, A&A, 577, A110
Zubko, V., Dwek, E., & Arendt, R. G. 2004, ApJS, 152, 211

Appendix A: Comparison with *Spitzer* + *Herschel* modelling of the Andromeda galaxy

The Andromeda galaxy is the nearest large spiral galaxy. It provides a useful benchmark to validate the current dust modelling. Its isophotal radius is $R_{25} = 95'$ (de Vaucouleurs et al. 1991), corresponding to $R_{25} = 20.6$ kpc at the assumed distance $d = 744$ kpc (Vilardell et al. 2010).

Several authors have modelled the dust properties of M31. Planck Collaboration Int. XXV (2015) presented an independent study to M31 using *Planck* maps and MBB dust model. In particular DA14 presented a DL based modelling of M31 using the IRAC (Fazio et al. 2004) and MIPS (Rieke et al. 2004) instruments on *Spitzer*, and the PACS (Poglitsch et al. 2010) and SPIRE (Griffin et al. 2010) instruments on *Herschel*. This data set has 13 photometric constraints (IRAC 3.6 μm, 4.5 μm, 5.8 μm, and 8.0 μm, MIPS 24 μm, 70 μm, and 160 μm, PACS 70 μm, 100 μm, and 160 μm, and SPIRE 250 μm, 350 μm, and 500 μm) from a different set of instruments than those used in our analysis. The high resolution modelling traces the structures of M31 in great detail, providing maps of $U_{\rm min}$ and dust surface density, and enables a comparison to be made with gas and metallicity observations. The modelling techniques are described and validated on NGC628 and NGC6946 in AD12, and later expanded to the full KINGFISH galaxy sample in AD15.

We compare the dust mass surface density maps[20] of the modelling presented by DA14 (from now on called "*Herschel*") degraded to a 5′ Gaussian PSF, with the current modelling, called "*Planck*". In the *Herschel* modelling, a tilted plane is fitted to the background areas, and subtracted from the original images to remove the Milky Way cirrus emission. Therefore, we need to add the cirrus emission back to the *Herschel* mass estimates before comparing to the *Planck* modelling. The zero level of the *Herschel* modelling was restored with an algorithm similar to that used to estimate the background planes in the KINGFISH dust modelling (see AD12). This algorithm iteratively fits an inclined plane to the difference in mass surface densities over the background points.

M31 does not have considerable quantities of cold dust, which would be detected in the *Planck* modelling but not in the *Herschel* modelling. Therefore, we expect both modellings to agree well.

Figure A.1 presents the comparison of the two dust models. The *Herschel* and *Planck* approaches agree very well: the resolved mass differences between the two analyses is small, only 10 % across most of the galaxy. The remaining parameter estimates also agree well. In conclusion, the model results appear not to be sensitive to the specific data sets used to constrain the FIR dust emission. This comparison validates the present modelling pipeline and methodology.

Appendix B: QSO A_V estimation

The intrinsic colours of an unobscured QSO depend strongly on its redshift[21] (ζ). We first estimate the (redshift dependent) unobscured QSO colour for each band pair. By comparing each QSO colours with the expected unobscured colours, we can estimate its reddening. Assuming a typical dust extinction curve, we can combine the reddening estimates of the band pairs into a single extinction estimate for each QSO. This analysis relies on the fact that the mean colour excess of a group of QSO scales linearly with the DL A_V estimates (see Figure B.2).

B.1. SDSS QSO catalogue

The SDSS is a photometric and spectroscopic survey, using a dedicated 2.5-m telescope at Apache Point Observatory in New Mexico. It has produced high quality observations of approximately 10^4 deg^2 of the northern sky in five optical and near IR bands: *u*, *g*, *r*, *i*, and *z*, centred at 354.3 nm, 477.0 nm, 623.1 nm, 762.5 nm, and 913.4 nm respectively (York et al. 2000). The SDSS seventh data release (DR7, Abazajian et al. 2009) contains a sample of 105 783 spectroscopically confirmed QSOs, and the SDSS tenth data release (DR10, Pâris et al. 2014) contains an additional sample of 166 583 QSOs.

[20] Both dust mass surface density maps correspond to the line of sight projected densities, not corrected for the M31 inclination.

[21] We will denote the QSO redshift as ζ, instead of the usual z to avoid confusion with the longest wavelength SDSS filter *z*.

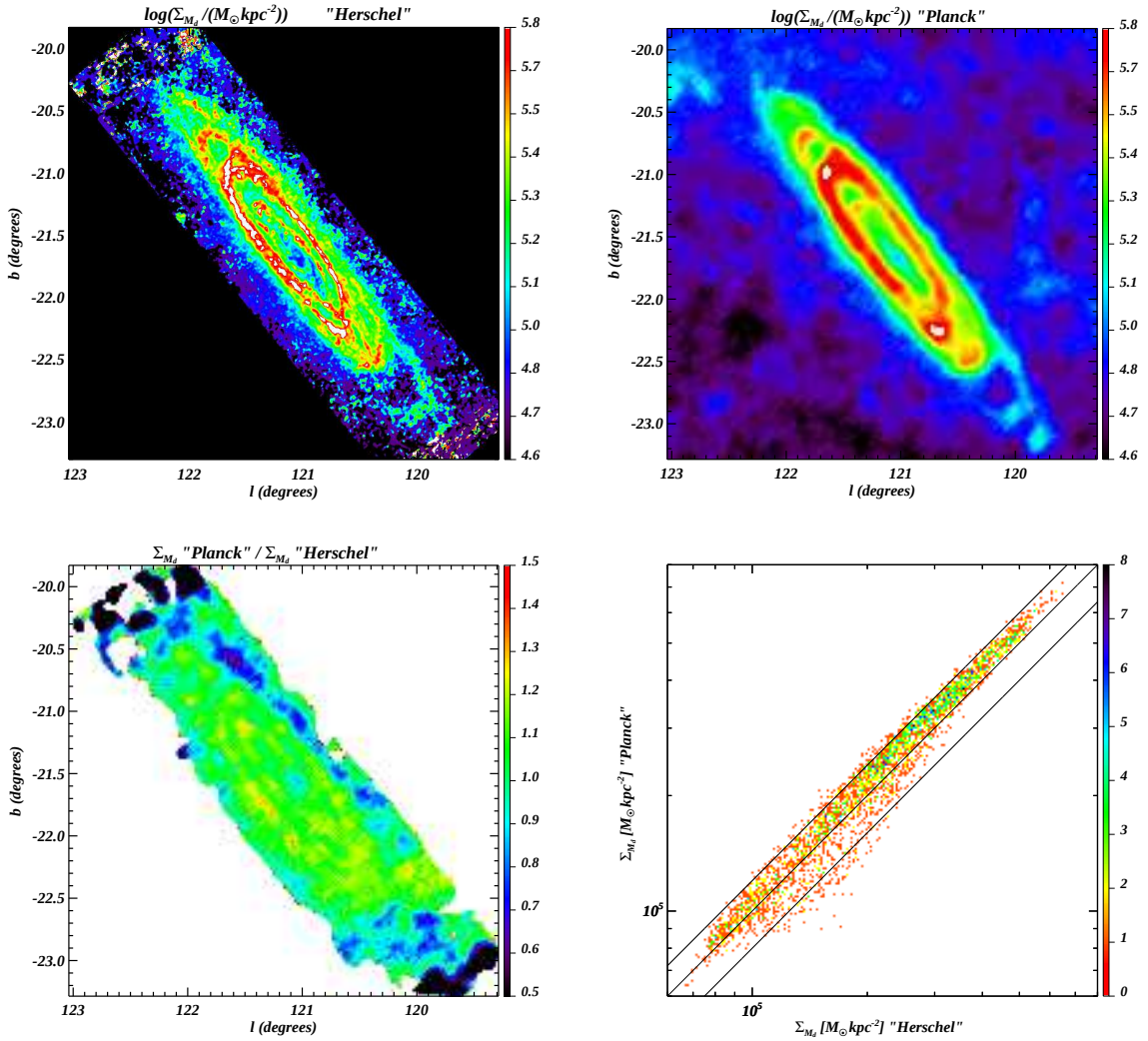

Fig. A.1. Comparison of M31 maps as seen by *Herschel* and *Planck*. The top row shows maps of the dust mass generated using *Spitzer* and *Herschel* data at high resolution (left) and the current estimates using *IRAS* and *Planck* data (right). The bottom row shows the ratio map of the two mass estimates (convolved to a common resolution and with the zero level matched) on the left, and their scatter on the right. The diagonal lines in the bottom right panel correspond to a one-to-one relationship and a ±20 % difference about that. The colour in the last panel corresponds to the density of points. Even though the two analyses are based on completely independent data, they agree remarkably well, differing by less than 10 % across most of the galaxy.

In order to avoid absorption from the intergalactic medium, each SDSS band is only usable up to the redshift at which the Lyα line (121.57 nm vacuum wavelength) enters (from the blue side) into the filter. Therefore, we can use the u-band, for QSOs with $\zeta < 1.64$, g-band for $\zeta < 2.31$, r-band for $\zeta < 3.55$, i-band for $\zeta < 4.62$, and z-band for $\zeta < 5.69$. We also limit the study to $0.35 < \zeta < 3.35$, to have enough QSOs per unit of redshift to estimate reliably the redshift-dependent unobscured QSO intrinsic colour (see Section B.2). We also remove the few QSOs that lie in a line of sight where the Galactic dust is very hot ($U_{\rm min} > 1.05$), very cold ($U_{\rm min} < 0.4$), very luminous ($L_{\rm dust} > 10^8 L_\odot$ kpc^{-2}), or where there is strong extinction ($A_V > 1$). This leaves 261 841 useful QSOs.

B.2. Unobscured QSO intrinsic colours and extinction estimation

A typical QSO spectrum has several emission and absorption lines superimposed on a power-law-like continuum. Depending on the QSO redshift, the lines fall in different filters. Therefore, for each optical band pair (X, Y), the unobscured QSO intrinsic colour $C_{X,Y}(\zeta)$ depends on the QSO redshift. Given two photometric bands X and Y, in order to estimate the unobscured QSO intrinsic colour $C_{X,Y}(\zeta)$, we proceed as follows.

We will see that the intrinsic dust properties appear to depend on the parameter $U_{\rm min}$. Therefore, to avoid introducing a potential bias when computing $C_{X,Y}(\zeta)$, we group the lines of sight according to $U_{\rm min}$, and analyse each group independently. The functions $C_{X,Y}(\zeta)$ should, in principle, not depend on $U_{\rm min}$, and therefore, all the estimates $C_{X,Y}(\zeta, U_{\rm min})$ should be similar for the different $U_{\rm min}$ sets. Working independently on each $U_{\rm min}$, for each redshift ζ we choose all the QSOs in the interval $[\zeta - 0.05, \zeta + 0.05]$, or the 2000 closest QSOs if there are more than 2000 QSOs in the interval, and fit the QSOs colour $(X - Y)$ as a function of the dust column density:

$$(X - Y) = C_{X,Y}(\zeta, U_{\rm min}) + \eta_{X,Y}(\zeta, U_{\rm min}) \times A_{V,\rm DL}, \qquad \text{(B.1)}$$

where $A_{V,\mathrm{DL}}$ is the DL estimated dust extinction in each QSO line of sight. The function $C_{X,Y}(\zeta, U_{\mathrm{min}})$ is the best estimate of the colour difference $(X-Y)$ of an unobscured QSO ($A_{V,\mathrm{DL}} = 0$) at redshift ζ, estimated from the lines of sight of dust fitted with U_{min}. The function $\eta_{X,Y}(\zeta, U_{\mathrm{min}})$ should be essentially independent of ζ[22]. Variations in the function $\eta_{X,Y}(\zeta, U_{\mathrm{min}})$ with respect to U_{min} give us information about the dust properties.

Once we compute $C_{X,Y}(\zeta, U_{\mathrm{min}})$ for the different values of U_{min}, we average them for each redshift ζ to obtain $C_{X,Y}(\zeta)$. For each U_{min} and ζ, the weight given to each $C_{X,Y}(\zeta, U_{\mathrm{min}})$ value is proportional to the number of QSO in the $[\zeta - 0.05, \zeta + 0.05]$ interval. Figure B.1 shows the results of this unobscured QSO intrinsic colour estimation algorithm for the bands i and z. The functions $C_{i,z}(\zeta, U_{\mathrm{min}})$ are shown for the different values of U_{min}, using redder lines for larger U_{min}, and greener for smaller U_{min}. Their weighted mean $C_{i,z}(\zeta)$ is shown in black.

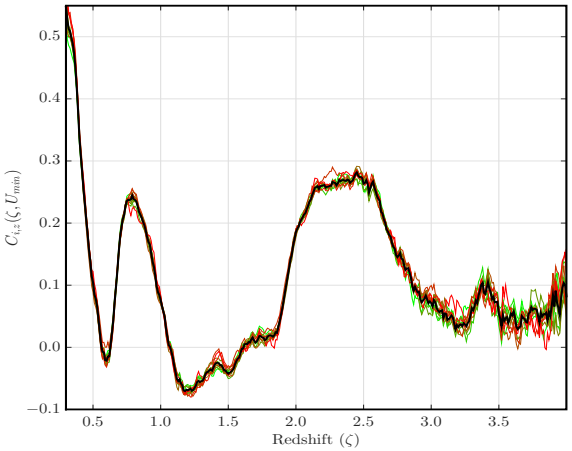

Fig. B.1. Unobscured QSO intrinsic colours, as a function of redshift (ζ), for the bands i and z. The functions $C_{i,z}(\zeta, U_{\mathrm{min}})$, are shown for the different values of U_{min}, using redder traces for larger U_{min}, and greener for smaller U_{min}. Their weighted mean $C_{i,z}(\zeta)$ is shown in black. The Lyα line affects the i band photometry for $\zeta > 4.62$, but we restrict our analysis to $\zeta < 3.35$ to have enough QSOs per redshift interval. For $\zeta > 3.35$ the estimated $C_{i,z}(\zeta)$ becomes noisy.

For each QSO, we define its reddening $E_{X,Y}$ as:

$$E_{X,Y} = (X - Y) - C_{X,Y}(\zeta). \tag{B.2}$$

The $E_{X,Y}$ values should not depend on the redshift, and therefore we can group all the QSOs of a given U_{min} into a sub sample with the same intrinsic colour. We note that no additional hypotheses on the QSO spectral shape or dust extinction curve need to be made to compute the QSO intrinsic colours. Working with all the QSOs with a given U_{min}, we fit

$$E_{X,Y} = \eta_{X,Y}(U_{\mathrm{min}}) \times A_{V,\mathrm{DL}}, \tag{B.3}$$

and identify the outlier QSOs that depart by more than $3\,\sigma$ from the expected linear relationship. Figure B.2 shows the typical QSO $E_{g,r}$ versus $A_{V,\mathrm{DL}}$ fit for $U_{\mathrm{min}} = 0.6$. In this case, $\eta_{g,r}(U_{\mathrm{min}} = 0.6) = 0.19$. Although the QSO $E_{X,Y}$ versus $A_{V,\mathrm{DL}}$ relationship has large scatter due to variations in the QSOs spectra (continuum and lines) and intrinsic obscuration in the QSOs, as long as there is no selection bias with respect to $A_{V,\mathrm{DL}}$ our study should be robust. The fact that the mean QSO $E_{X,Y}$ for each $A_{V,\mathrm{DL}}$ (curve) and the best fit of the QSO $E_{X,Y}$ versus $A_{V,\mathrm{DL}}$ (straight line) in Figure B.2 agree remarkably well, supports the validity of the preceding analysis.

[22] See the discussion following Eq. B.6.

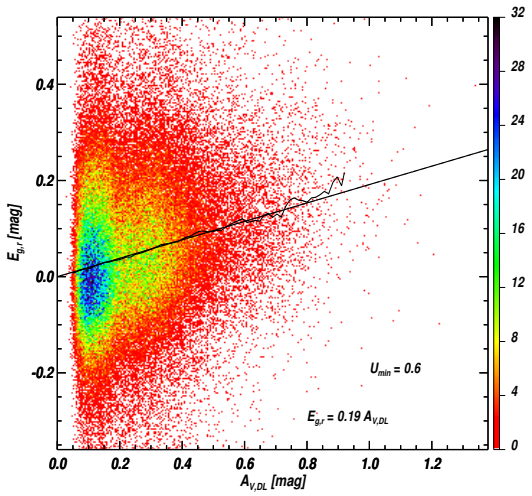

Fig. B.2. Colour excess $E_{g,r}$ versus $A_{V,\mathrm{DL}}$ for the QSOs with $U_{\mathrm{min}} = 0.6$. Colour corresponds to the density of points (see Figure 5). The straight line corresponds to the best fit for all the QSOs. For each $A_{V,\mathrm{DL}}$, the black curve corresponds to the mean $E_{g,r}$ for the QSOs in an interval with a half-width $\delta A_{V,\mathrm{DL}} = 0.01$. Even though the QSOs show significant scatter, the $E_{g,r}$ versus $A_{V,\mathrm{DL}}$ relationship is very linear; the mean $E_{g,r}$ for each $A_{V,\mathrm{DL}}$ curve does not show significant departures from the straight line.

Once we have computed $E_{X,Y}$ for all the band pairs and U_{min}, we remove the QSOs that are considered as outliers in any of the computations to obtain a cleaner sample of good QSOs. We reiterate the full procedure twice using the good QSO sample form the previous iteration, resulting in a final cleanest sample containing 224 245 QSOs with $\zeta < 3.35$ (for which we have Lyα free photometry in the r-, i-, and z-bands), 135,953 with $\zeta < 2.31$ (where we can use the r-band), and 77 633 QSO with $\zeta < 1.64$, where we can use all the SDSS bands. We have an estimate of the intrinsic colours $C_{X,Y}$, and an estimate of the reddening $E_{X,Y}$ for each QSO that is retained by the redshift constraints.

Even though the unobscured QSO intrinsic colours are computed independently for each band pair, we do obtain consistent results across the band pairs, i.e.

$$C_{X,Y}(\zeta) - C_{Y,Z}(\zeta) \approx C_{X,Z}(\zeta), \tag{B.4}$$

holds for all the bands X, Y, and Z, over all the redshifts ζ considered. Working with the H I column density maps as an estimate of the extinction instead of the $A_{V,\mathrm{DL}}$ gives very similar estimates of $C_{X-Y}(\zeta)$, and is independent of any dust modelling, so this means we did not translate potential dust modelling systematics into our QSO estimates.

In order to compare the $A_{V,\mathrm{DL}}$ estimate with a QSO estimate, we need to derive a QSO extinction A_V from the different colour excess $E_{X,Y}$. We proceed as follows.

For a given QSO spectrum and extinction curve shape, we can compute the SDSS magnitude increase per dust extinction A_X/A_V for $X = u$, g, r, i, and z. These ratios depend on the assumed extinction curve and QSO spectral shape, and therefore on the QSO redshift. Using the QSO composite spectrum of Vanden Berk et al. (2001) and the extinction curve presented by Fitzpatrick (1999) parametrized via R_V, we compute the ratios

A_X/A_V:

$$\delta X(\zeta, R_V) \equiv A_X/A_V. \quad \text{(B.5)}$$

Figure B.3 shows $\delta X(\zeta, R_V = 3.1)$ as a function of the QSO redshift ζ, for the different bands $X = u$, g, r, i, and z. Even though the QSO intrinsic colours are strong functions of its redshift, the extinction curves are smooth enough that $\delta X(\zeta, R_V = 3.1)$ is mostly redshift independent.

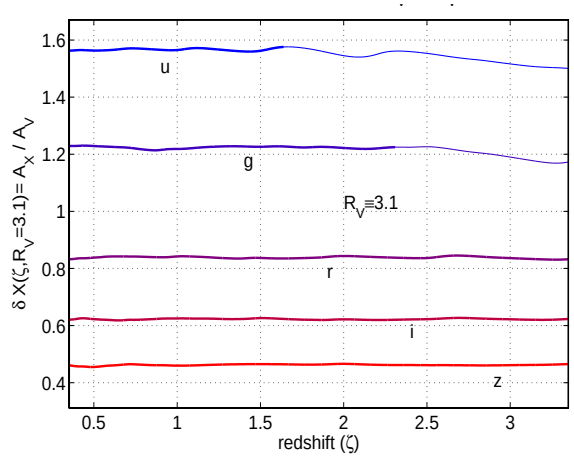

Fig. B.3. QSO magnitude increase per unit of dust extinction A_V as a function of the QSO redshift. We use an extinction curve with $R_V = 3.1$. The u and g band curves are shown in a thinner trace for $\zeta > 1.64$ and $\zeta > 2.31$, the redshifts at which the intergalactic Lyα line can affect the photometry in these bands.

Using the extinction curves with $R_V = 3.1$ (which was also used to constrain the optical properties of the grains used in the DL model), for each redshift ζ, we define:

$$\delta_{[X,Y]}(\zeta) = \frac{1}{\delta X(\zeta, R_V = 3.1) - \delta Y(\zeta, R_V = 3.1)}, \quad \text{(B.6)}$$

and

$$A_{V,\mathrm{QSO},[X,Y]} = \delta_{[X,Y]} \times E_{X,Y}. \quad \text{(B.7)}$$

Finally, for each QSO, we define its $A_{V,\mathrm{QSO}}$ as the average of the $A_{V,\mathrm{QSO},[X,Y]}$ values for all the band pairs that are allowed by its redshift ζ.

Appendix C: Impact of the CIB anisotropies and instrumental noise on the parameter estimation

We study the impact of CIB anisotropies (CIBA) and instrumental (stochastic) noise in our mass estimates in the diffuse ISM (where their effect should be the largest). We simulate data by adding CIBA and instrumental noise to DL SEDs, and fit them with the same technique as we use to fit the observed data. The results quantify the deviations of the recovered parameters from the original ones.

We start by a family of four DL SEDs with $U_{\mathrm{min}} = 0.4$, 0.6, 0.8, and 1.0, a typical $f_{\mathrm{PDR}} = 0.05$, and $q_{\mathrm{PAH}} = 0.03$. We normalize each SED to the mean A_V found for the QSO lines of sight in each U_{min}. We replicate each SED 100 000 times, add CIB anisotropies and instrumental noise. The noise added has 2 components. We add (band-to-band) independent noise to simulate stochastic instrumental noise with amplitudes given by *Pl*-MBB, Table B.1, 30′ resolution. We further add a typical CIB SED (also from *Pl*-MBB, Table B.1, 30′ row), that is completely correlated across the *Planck* bands, and partially correlated with the *IRAS* bands, as recommended in *Pl*-MBB, Appendix B. We finally fit each simulated SED with DL model, as we did in the main data fit.

Figure C.1 shows the recovered Σ_{M_d} divided by the original Σ_{M_d}, and recovered U_{min} for the SEDs. Each set of points correspond to the different original U_{min}. The inclined solid line corresponds to the renormalization curve given by Eq. 9, (rescaled to match the mean A_V of the simulated SEDs). There is not a global bias in the recovered Σ_{M_d}, nor U_{min}; the distribution of the recovered Σ_{M_d} and U_{min} are centered in the original values. Although CIBA and instrumental noise do generate a trend in the same direction as the renormalization, their impact is significantly smaller than the observed renormalization: they do not span the full range found over the QSOs lines of sight. Moreover, the renormalization found in Section 6.3 is independent of the modelling resolution; one obtain similar renormalization coefficients working at 5′, 30′, and 60′ FWHM. For those resolutions, the instrumental noise and CIBA have a very different magnitude, and therefore, their impact would be quite different. Therefore, CIBA and instrumental noise are not a significant source of the A_V systematic departures with respect to U_{min} found in Section 6.3.

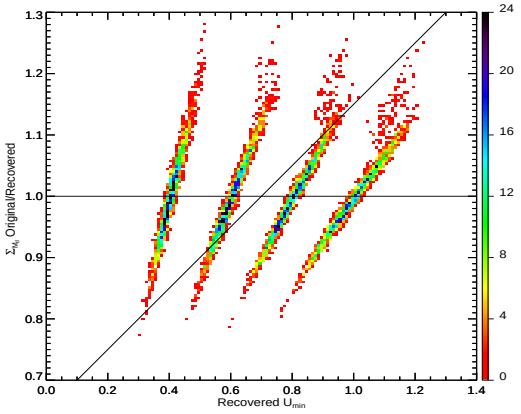

Fig. C.1. Comparison of the original and recovered dust mass under CIBA and instrumental noise simulation in the diffuse ISM for a 30′ resolution. Colour corresponds to the density of points (see Figure 5).

Appendix D: Maps in the Planck Legacy Archive

The maps of the dust model parameters, the dust extinction and the model predicted fluxes described in this paper can be obtained from the Planck Legacy Archive (PLA).[23] The maps are all at 5′(FWHM) angular resolution in the `HEALPix` representation with $N_{\mathrm{side}} = 2\,048$.

For each quantity, but the χ^2 of the fit per degree of freedom, there are 2 maps corresponding to the value presented and the corresponding uncertainty. Available maps include our best estimate of the dust extinction (the renormalized $A_{V,\mathrm{RQ}}$) expressed in magnitude units, and the best fit DL parameters: the dust mass surface density Σ_{M_d} expressed in $\mathrm{M}_\odot\,\mathrm{kpc}^{-2}$ units, the starlight intensity heating the bulk of the dust, U_{min} in units of the ISRF estimated by Mathis et al. (1983) for the solar neighbourhood,

[23] `http://pla.esac.esa.int/pla/`

the fraction of the dust luminosity from dust heated by intense radiation fields, $f_{\rm PDR}$ in Eq. 2, which is a dimensionless number between 0 and 1, and the dust mass fraction in small PAH grains $q_{\rm PAH}$. We also provide the DL model predicted fluxes in the *Planck*, *IRAS* 60 and 100, and *WISE* 12 bands. Additional information about the file names and the data format is available in the *Planck* explanatory supplement[24].

[1] APC, AstroParticule et Cosmologie, Université Paris Diderot, CNRS/IN2P3, CEA/lrfu, Observatoire de Paris, Sorbonne Paris Cité, 10, rue Alice Domon et Léonie Duquet, 75205 Paris Cedex 13, France

[2] African Institute for Mathematical Sciences, 6-8 Melrose Road, Muizenberg, Cape Town, South Africa

[3] Agenzia Spaziale Italiana Science Data Center, Via del Politecnico snc, 00133, Roma, Italy

[4] Agenzia Spaziale Italiana, Viale Liegi 26, Roma, Italy

[5] Astrophysics Group, Cavendish Laboratory, University of Cambridge, J J Thomson Avenue, Cambridge CB3 0HE, U.K.

[6] Astrophysics & Cosmology Research Unit, School of Mathematics, Statistics & Computer Science, University of KwaZulu-Natal, Westville Campus, Private Bag X54001, Durban 4000, South Africa

[7] Atacama Large Millimeter/submillimeter Array, ALMA Santiago Central Offices, Alonso de Cordova 3107, Vitacura, Casilla 763 0355, Santiago, Chile

[8] CITA, University of Toronto, 60 St. George St., Toronto, ON M5S 3H8, Canada

[9] CNRS, IRAP, 9 Av. colonel Roche, BP 44346, F-31028 Toulouse cedex 4, France

[10] California Institute of Technology, Pasadena, California, U.S.A.

[11] Centro de Estudios de Física del Cosmos de Aragón (CEFCA), Plaza San Juan, 1, planta 2, E-44001, Teruel, Spain

[12] Computational Cosmology Center, Lawrence Berkeley National Laboratory, Berkeley, California, U.S.A.

[13] Consejo Superior de Investigaciones Científicas (CSIC), Madrid, Spain

[14] DSM/Irfu/SPP, CEA-Saclay, F-91191 Gif-sur-Yvette Cedex, France

[15] DTU Space, National Space Institute, Technical University of Denmark, Elektrovej 327, DK-2800 Kgs. Lyngby, Denmark

[16] Département de Physique Théorique, Université de Genève, 24, Quai E. Ansermet,1211 Genève 4, Switzerland

[17] Departamento de Física, Universidad de Oviedo, Avda. Calvo Sotelo s/n, Oviedo, Spain

[18] Department of Astrophysics/IMAPP, Radboud University Nijmegen, P.O. Box 9010, 6500 GL Nijmegen, The Netherlands

[19] Department of Physics & Astronomy, University of British Columbia, 6224 Agricultural Road, Vancouver, British Columbia, Canada

[20] Department of Physics and Astronomy, Dana and David Dornsife College of Letter, Arts and Sciences, University of Southern California, Los Angeles, CA 90089, U.S.A.

[21] Department of Physics and Astronomy, University College London, London WC1E 6BT, U.K.

[22] Department of Physics, Florida State University, Keen Physics Building, 77 Chieftan Way, Tallahassee, Florida, U.S.A.

[23] Department of Physics, Gustaf Hällströmin katu 2a, University of Helsinki, Helsinki, Finland

[24] Department of Physics, Princeton University, Princeton, New Jersey, U.S.A.

[25] Department of Physics, University of California, Santa Barbara, California, U.S.A.

[26] Department of Physics, University of Illinois at Urbana-Champaign, 1110 West Green Street, Urbana, Illinois, U.S.A.

[27] Dipartimento di Fisica e Astronomia G. Galilei, Università degli Studi di Padova, via Marzolo 8, 35131 Padova, Italy

[28] Dipartimento di Fisica e Scienze della Terra, Università di Ferrara, Via Saragat 1, 44122 Ferrara, Italy

[29] Dipartimento di Fisica, Università La Sapienza, P. le A. Moro 2, Roma, Italy

[30] Dipartimento di Fisica, Università degli Studi di Milano, Via Celoria, 16, Milano, Italy

[31] Dipartimento di Fisica, Università degli Studi di Trieste, via A. Valerio 2, Trieste, Italy

[32] Dipartimento di Fisica, Università di Roma Tor Vergata, Via della Ricerca Scientifica, 1, Roma, Italy

[33] Discovery Center, Niels Bohr Institute, Blegdamsvej 17, Copenhagen, Denmark

[34] Dpto. Astrofísica, Universidad de La Laguna (ULL), E-38206 La Laguna, Tenerife, Spain

[35] European Southern Observatory, ESO Vitacura, Alonso de Cordova 3107, Vitacura, Casilla 19001, Santiago, Chile

[36] European Space Agency, ESAC, Planck Science Office, Camino bajo del Castillo, s/n, Urbanización Villafranca del Castillo,

[24] `http://wiki.cosmos.esa.int/planckpla2015/`

Villanueva de la Cañada, Madrid, Spain

[37] European Space Agency, ESTEC, Keplerlaan 1, 2201 AZ Noordwijk, The Netherlands

[38] Facoltà di Ingegneria, Università degli Studi e-Campus, Via Isimbardi 10, Novedrate (CO), 22060, Italy

[39] HGSFP and University of Heidelberg, Theoretical Physics Department, Philosophenweg 16, 69120, Heidelberg, Germany

[40] Helsinki Institute of Physics, Gustaf Hällströmin katu 2, University of Helsinki, Helsinki, Finland

[41] INAF - Osservatorio Astrofisico di Catania, Via S. Sofia 78, Catania, Italy

[42] INAF - Osservatorio Astronomico di Padova, Vicolo dell'Osservatorio 5, Padova, Italy

[43] INAF - Osservatorio Astronomico di Roma, via di Frascati 33, Monte Porzio Catone, Italy

[44] INAF - Osservatorio Astronomico di Trieste, Via G.B. Tiepolo 11, Trieste, Italy

[45] INAF/IASF Bologna, Via Gobetti 101, Bologna, Italy

[46] INAF/IASF Milano, Via E. Bassini 15, Milano, Italy

[47] INFN, Sezione di Bologna, Via Irnerio 46, I-40126, Bologna, Italy

[48] INFN, Sezione di Roma 1, Università di Roma Sapienza, Piazzale Aldo Moro 2, 00185, Roma, Italy

[49] INFN/National Institute for Nuclear Physics, Via Valerio 2, I-34127 Trieste, Italy

[50] IPAG: Institut de Planétologie et d'Astrophysique de Grenoble, Université Grenoble Alpes, IPAG, F-38000 Grenoble, France, CNRS, IPAG, F-38000 Grenoble, France

[51] Imperial College London, Astrophysics group, Blackett Laboratory, Prince Consort Road, London, SW7 2AZ, U.K.

[52] Infrared Processing and Analysis Center, California Institute of Technology, Pasadena, CA 91125, U.S.A.

[53] Institut Universitaire de France, 103, bd Saint-Michel, 75005, Paris, France

[54] Institut d'Astrophysique Spatiale, CNRS (UMR8617) Université Paris-Sud 11, Bâtiment 121, Orsay, France

[55] Institut d'Astrophysique de Paris, CNRS (UMR7095), 98 bis Boulevard Arago, F-75014, Paris, France

[56] Institute for Space Sciences, Bucharest-Magurale, Romania

[57] Institute of Astronomy, University of Cambridge, Madingley Road, Cambridge CB3 0HA, U.K.

[58] Institute of Theoretical Astrophysics, University of Oslo, Blindern, Oslo, Norway

[59] Instituto de Astrofísica de Canarias, C/Vía Láctea s/n, La Laguna, Tenerife, Spain

[60] Instituto de Física de Cantabria (CSIC-Universidad de Cantabria), Avda. de los Castros s/n, Santander, Spain

[61] Jet Propulsion Laboratory, California Institute of Technology, 4800 Oak Grove Drive, Pasadena, California, U.S.A.

[62] Jodrell Bank Centre for Astrophysics, Alan Turing Building, School of Physics and Astronomy, The University of Manchester, Oxford Road, Manchester, M13 9PL, U.K.

[63] Kavli Institute for Cosmology Cambridge, Madingley Road, Cambridge, CB3 0HA, U.K.

[64] LAL, Université Paris-Sud, CNRS/IN2P3, Orsay, France

[65] LERMA, CNRS, Observatoire de Paris, 61 Avenue de l'Observatoire, Paris, France

[66] Laboratoire AIM, IRFU/Service d'Astrophysique - CEA/DSM - CNRS - Université Paris Diderot, Bât. 709, CEA-Saclay, F-91191 Gif-sur-Yvette Cedex, France

[67] Laboratoire Traitement et Communication de l'Information, CNRS (UMR 5141) and Télécom ParisTech, 46 rue Barrault F-75634 Paris Cedex 13, France

[68] Laboratoire de Physique Subatomique et de Cosmologie, Université Joseph Fourier Grenoble I, CNRS/IN2P3, Institut National Polytechnique de Grenoble, 53 rue des Martyrs, 38026 Grenoble

cedex, France

[69] Laboratoire de Physique Théorique, Université Paris-Sud 11 & CNRS, Bâtiment 210, 91405 Orsay, France

[70] Lawrence Berkeley National Laboratory, Berkeley, California, U.S.A.

[71] Max-Planck-Institut für Astrophysik, Karl-Schwarzschild-Str. 1, 85741 Garching, Germany

[72] McGill Physics, Ernest Rutherford Physics Building, McGill University, 3600 rue University, Montréal, QC, H3A 2T8, Canada

[73] National University of Ireland, Department of Experimental Physics, Maynooth, Co. Kildare, Ireland

[74] Niels Bohr Institute, Blegdamsvej 17, Copenhagen, Denmark

[75] Observational Cosmology, Mail Stop 367-17, California Institute of Technology, Pasadena, CA, 91125, U.S.A.

[76] Princeton University Observatory, Peyton Hall, Princeton, NJ 08544-1001, U.S.A.

[77] SISSA, Astrophysics Sector, via Bonomea 265, 34136, Trieste, Italy

[78] School of Physics and Astronomy, Cardiff University, Queens Buildings, The Parade, Cardiff, CF24 3AA, U.K.

[79] Space Research Institute (IKI), Russian Academy of Sciences, Profsoyuznaya Str, 84/32, Moscow, 117997, Russia

[80] Space Sciences Laboratory, University of California, Berkeley, California, U.S.A.

[81] Special Astrophysical Observatory, Russian Academy of Sciences, Nizhnij Arkhyz, Zelenchukskiy region, Karachai-Cherkessian Republic, 369167, Russia

[82] Sub-Department of Astrophysics, University of Oxford, Keble Road, Oxford OX1 3RH, U.K.

[83] UPMC Univ Paris 06, UMR7095, 98 bis Boulevard Arago, F-75014, Paris, France

[84] Université de Toulouse, UPS-OMP, IRAP, F-31028 Toulouse cedex 4, France

[85] Universities Space Research Association, Stratospheric Observatory for Infrared Astronomy, MS 232-11, Moffett Field, CA 94035, U.S.A.

[86] University of Granada, Departamento de Física Teórica y del Cosmos, Facultad de Ciencias, Granada, Spain

[87] University of Granada, Instituto Carlos I de Física Teórica y Computacional, Granada, Spain

[88] Warsaw University Observatory, Aleje Ujazdowskie 4, 00-478 Warszawa, Poland